INVESTIGATION OF ULTEM 9085 FOR USE IN 3-D PRINTED ORBITAL STRUCTURES

THESIS

William R. Gallagher, Civ, USAF

AFIT-ENY-MS-20-M-262

DEPARTMENT OF THE AIR FORCE
AIR UNIVERSITY

AIR FORCE INSTITUTE OF TECHNOLOGY

Wright-Patterson Air Force Base, Ohio

AFIT-ENY-MS-20-M-262

INVESTIGATION OF ULTEM 9085 FOR USE IN 3-D PRINTED ORBITAL STRUCTURES

THESIS

Presented to the Faculty

Department of Aeronautics And Astronautics

Graduate School of Engineering and Management

Air Force Institute of Technology

Air University

Air Education and Training Command

in Partial Fulfillment of the Requirements for the

Degree of Master of Science in Astronautical Engineering

William R. Gallagher, B.S.A.E.

Civ, USAF

March 26, 2020

AFIT-ENY-MS-20-M-262

INVESTIGATION OF ULTEM 9085 FOR USE IN 3-D PRINTED ORBITAL STRUCTURES

William R. Gallagher, B.S.A.E.
Civ, USAF

Committee Membership:

Dr. Carl Hartsfield, PhD
Chair

Maj Joshuah Hess, PhD
Member

Maj Ryan Kemnitz, PhD
Member

Abstract

Additive manufacturing is revolutionizing industries ranging from medicine to space. However, the structural characteristics of plastic parts created by these methods are not as well understood as their more established counterparts. This research explored two relevant areas: how the structural characteristics of ULTEM 9085 plastic behaved after exposure to orbital conditions and the design of the cross-sectional area of a beam to be 3-D printed in microgravity based on the expected loads from the printer.

To study orbital effects, ULTEM 9085 was printed into 1/4th scale ASTM D638-14 dogbones using a Stratasys 450mc printer. These dogbones were placed in a vacuum chamber and exposed to ultraviolet (UV) radiation and high temperatures. The dogbones were removed regularly from the testing environments after up to 980 hours in the chamber and subjected to axial loading tests using an MTS Microtester. Using the initial shape of the dogbones and the collected force values, the stress-strain curve for each sample in each exposure duration was found, and the Young's modulus, Ultimate Tensile Strength (UTS), Yield Tensile Strength (YTS), Poisson's ratio, and Fracture Strain calculated. The ULTEM 9085 became stronger as a result of the vacuum and more brittle as a result of the UV radiation.

Simultaneously, data from previous studies into ULTEM 9085's structural characteristics was imported into Hyperworks' Optistruct software module. The data was used to optimize a beam's internal structure based on several possible loading configurations expected during printing on orbit. A general design was selected and its maximum allowable end moment was found. The above information will be helpful in designing ULTEM 9085 structures for use on orbit.

Acknowledgments

I must first thank the PALACE Acquire Program for agreeing to let me study at AFIT. I have seen more and gone farther than I would have anywhere else, *per audacia ad astra*. Dr. Carl Hartsfield, thank you for the help and insights necessary to complete this research. Travis Shelton and Maj Ryan Kemnitz, thank you for helping operate the equipment and your knowledge during the research and publication process. Josh DeWitt, Jamie Smith, and Michael Ranft, thank you for all your help and for keeping everything running.

Blessed Saint Leibowitz, keep 'em dreamin' down there.

-Col Randy Claggett, *Space*

William R. Gallagher

Table of Contents

Page

List of Figures

Figure Page

List of Tables

List of Acronyms

μm micrometers

°C Celsius

AFIT Air Force Institute of Technology

AM Additive Manufacturing

cm centimeters

COTS Commercial Off-The-Shelf

CoV Coefficient of Variance

FDM Fused Deposition Modeling

FoS Factor of Safety

IR Infared

ISS International Space Station

K Kelvin

km kilometers

kN kiloNewton

kN-m kiloNewton meters

LEO Low Earth Orbit

m meter

mm millimeters

MPa MegaPascals

MTS MTS 250 Tytron Microtester

N Newton

SIMP Solid Isotropic Material with Penalization

SVC Small Vacuum Chamber

UTS Ultimate Tensile Strength

UV Ultraviolet

W Watt

Xe Xenon

YTS Yield Tensile Strength

List of Symbols

$\bar{K}$	Penalized Stiffness Matrix
γ	Earth's Angular Radius
ν	Poisson's ratio
ρ	Normalized Density
σ_v	Von Mises Stress
σ_{xy}	Stress in the given direction
τ	Shear Stress
$\mathbf{k}_e$	Element Stiffness Matrix
$\mathbf{u}_e$	Element Displacement Vector
E	Eclipse Fraction Time
f	Volume Fraction
H	Altitude
K	Local Stiffness Matrix
N_{el}	Number of Elements
p	Penalization Power
R_E	Earth's Radius
$V(x)$	Volume
V_0	Original Volume
x	Design Variable Vector
x_{min}	Minimum Non-Zero Design Variable Vector
λ	Wavelength
σ	Stefan–Boltzmann Constant
$\mathbf{F}$	Global Force Vector
$\mathbf{K}$	Global Stiffness Matrix
$\mathbf{U}$	Global Displacement Vector
E_b	Emissive Power
I	Moment of Inertia
Q	Statical Moment of Area
r	Radius
T	Temperature
V	Shear Force

INVESTIGATION OF ULTEM 9085 FOR USE IN 3-D PRINTED ORBITAL STRUCTURES

I. Introduction

1.1 Background

While Additive Manufacturing (AM) has existed in some form for several decades, the first patent for what is recognizable as AM today was not filed with the Patent Office until 1984 [1]. Since then, parts produced by AM have been used in industries ranging from space to hobbyist interests. Continued improvements in AM mean these parts will become more common as the 21st century progresses [2]. However, one key problem facing wider implementation is the inconsistency of structural characteristics of parts produced by AM. This is especially true for parts produced by Fused Deposition Modeling (FDM), a method that will be discussed in detail later. Previous research has shown that variations in printing temperature and direction noticeably change the structural characteristics of FDM parts [3].

Recently, the installation of Made-in-Space's 3-D printer on the International Space Station (ISS) [4] and the launch of a FDM cubesat from the ISS [5] demonstrates there is interest in AM parts for space applications. ULTEM 9085 is an ideal material for use in outer space as it undergoes little outgassing in a vacuum and has a high glass transition temperature [6]. But there has been little research into how the orbital environment will affect the structural characteristics of printed ULTEM 9085 plastic. Structural studies done on plastics in an orbital environment have been on plastics created via traditional manufacturing methods.

Simultaneously, the Air Force Institute of Technology (AFIT) has begun designing an autonomous 3-D printer that will print satellite structural components on orbit. The goal is to reduce the mass of the satellite, since components printed on orbit will not need to survive launch conditions and can be custom designed based on mission needs. However, these studies have only looked at the printer's architecture [7].

1.2 Research Focus

Designing long-life parts is impossible if designers cannot predict how the parts will behave over that life. ULTEM 9085's applicability for usage in space is impeded by this knowledge gap. Further, if ULTEM 9085 is to be printed in an orbital environment, it is essential to know what kind of design will be best for printing based on current microgravity printer designs.

This leads to two topics for research:

- How does UTLEM 9085's structural behavior change with exposure to Ultraviolet (UV) radiation, elevated temperatures, and vacuum? Are there any structural characteristics a function of exposure to UV radiation only?
- What is the ideal internal topology for a 3-D printed structural tube created by AFIT's vacuum 3-D printer to support expected types of loading due to the printer during orbital operations?

1.3 Methodology/Equipment/Software

For testing the ULTEM 9085, FDM-printed dogbones were exposed to high levels of UV radiation inside a vacuum chamber. An equal number of dogbones were shielded from UV radiation in the chamber as well. The dogbones were removed periodically and subjected to axial loading, the resulting data used to calculate the Ultimate

Tensile Strength (UTS), Yield Tensile Strength (YTS), Young's modulus, Poisson's ratio, and Fracture Strain.

For designing the beam, the maximum allowable shear stress for a solid cylinder was calculated. The required shear loading resulting in said stress were calculated and applied to a model in Hyperworks. The model was then optimized several times for several possible loading configurations to create an average topology. The largest moment this new shape could withstand while undergoing the shear stresses was then found.

The key equipment used in this research was a Stratasys Fortus 450mc printer, a MTS 250 Tytron Microtester, AFIT's Small Vacuum Chamber (SVC), a Zeiss Discovery V.12 SteREO optical microscope, a Newport UV source, and a Thorlabs Optical Power and Energy Meter with associated Thermal Power Sensor. The software used included Zeiss ZEN Core, LabView, MTS Operations, the Hyperview and Optistruct packages in Hyperworks, and Solidworks.

1.4 Assumptions

All testing was done on samples of Commercial Off-The-Shelf (COTS) UTLEM 9085 printed on a COTS Stratasys printer. The lot/batch number of the ULTEM 9085 was not recorded, nor if there were irregularities while printing the samples. Any variations during UV exposure were assumed to be linear and blackbody assumptions were applied where needed.

For analysis of the beam, the allowable shear forces were calculated assuming pure shear on a beam 1 meter (m) long with a Factor of Safety (FoS) of 2, and the resulting allowable moment derived from the Von Mises criteria. The analysis was done assuming the member was isotropic using minimum strength characteristics from previous AFIT research [3].

1.5 Preview

- Chapter I: Outlines the purpose of this thesis, detailing the exact questions to be answered, the hardware and procedure to do so, and the underlying assumptions.
- Chapter II: Discusses previous research into the effects of orbital exposure on plastics and how this research fits into it.
- Chapter III: Provides a detailed explanation of how the experiments and analysis were carried out.
- Chapter IV: Collects and analyzes the results of the experiment and analysis.
- Chapter V: Draws conclusions and discusses where to take further research.

II. Literature Review

2.1 Fused Deposition Modeling

While there are several Additive Manufacturing (AM) processes in use commercially, this research will focus exclusively on Fused Deposition Modeling (FDM). During the FDM process, fibers of almost-melted thermoplastic are sequentially layered into a desired 3-D shape by a heated nozzle. The position and pattern the nozzle follows is controlled by the software that the desired part is uploaded into. If necessary, support material is included to prevent the part from deforming until it has sufficiently cooled [8]. The Commercial Off-The-Shelf (COTS) printer used in this research was a FORTUS 450mc, which deposits UTLEM 9085 in layers 0.254 mm thick [9].

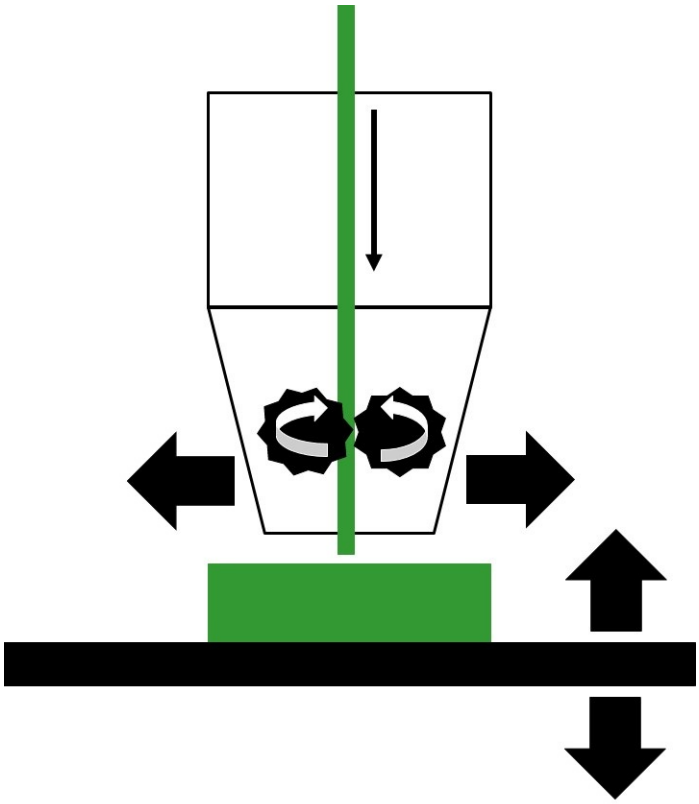

Figure 2.1. How an FDM printer positions the nozzle to layer the thermoplastic fibers.

Figure 2.2. The FORTUS 450mc Printer used to create the test samples.

One unique detail of FDM parts is that they are anisotropic. While the raw thermoplastics used in the process are isotropic, the printing process causes anistropy. The fibers of plastic are typically layered in what is called a raster fill. The outline of a given layer is printed first and the interior then filled with a back and forth pattern angled at 45°. The subsequent layer's fill is then perpendicular to the previous one and the pattern repeated until the required height is met [10]. Depending on the printer's operating parameters, this can result in air gaps between fibers in a layer or between the layers, in some cases the fibers may not be hot long enough to merge into the gaps.

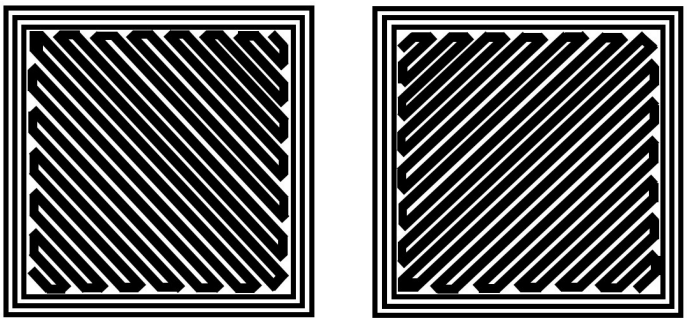

Figure 2.3. Raster fill pattern typical of FDM printing.

FDM is uniquely applicable to space because it does not rely on gravity to work. Other AM processes require a powdered or liquid base material, used to create a part by sintering or solidifying the base into a specific shape. Further, UTLEM 9085's high melting point and minimal outgassing makes it ideal for use in an orbital environment. A COTS FDM printer's nozzle can be modified to keep the ULTEM 9085 at the needed temperature in a vacuum long enough to print a viable part [11], showing ULTEM 9085 parts can be manufactured on orbit. Previous research at Air Force Institute of Technology (AFIT) has focused on FDM for this reason, specifically theses written by 2d Lt Zane Wilburn, 2d Lt John P. McCrea, and Capt Joshua T. Cerri, all of which served as a foundation for this thesis.

2.2 Orbital Conditions

Since not all aspects of the Low Earth Orbit (LEO) environment can be re-created in a vacuum chamber, three aspects of the LEO environment were focused on here, elevated temperatures, vacuum, and Ultraviolet (UV) radiation exposure. While these conditions, especially UV exposure, have been studied extensively [12], these studies have been done on plastics made by traditional manufacturing methods. Because FDM parts are made from re-heated plastic in varying arrangements, the assumptions and findings from these studies may not apply to different shapes or to ULTEM made in a different printer. Understanding how FDM parts will behave will require a reexamination, but not dismissal, of known plastic behaviors.

2.2.1 Vacuum and Temperature

How temperature affects the ULTEM 9085 parts is especially important given the FDM process requires the plastic to almost melt. Testing UTLEM 9085 printed at various temperatures revealed that failure occurred where the fibers met and that

the strength of the UTLEM 9085 improved at higher printing temperatures [3]. A change in temperature may not only affect the UTLEM 9085 fibers, but how the fibers stay adhered to one another. It is logical to assume that extended time at elevated temperatures would cause a change in structural characteristics, though not for the same reasons as in Willburn's research.

Further, studies have shown temperatures of 26 to 260 Celsius (°C) and vacuum conditions of approximately 3E-7 Torr do cause polycarbonates and fluorocarbons to lose material [13]. While this thermal vacuum experiment was done on Lexan and Teflon, they are both organic, carbon-centered thermoplastics like ULTEM 9085. Combined with heat effects, it would be expected that the UTLEM 9085 loses material but gains structural strength due to a heated vacuum environment, with the fracturing occurring where the fibers meet.

2.2.2 UV Radiation

Traditionally-manufactured plastics become brittle when exposed to sunlight for an extended duration, upward of 1,000 hours. This also happens in composite materials with polymers in them, with the most damaging effects occurring at temperatures above 100 °C [14]. While relevant information, usual terrestrial temperatures are not that elevated and the UV radiation must pass through absorbing gasses like ozone before reaching the Earth's surface, which filter out most of the energy in the wavelengths below 0.4 micrometers (μm) [15]. LEO has a much wider range of temperatures and no natural UV filtering.

Conversely, UV radiation has also been shown to harden other plastics. Leaving polyurethane exposed to the soft UV radiation typical at the Earth's surface will increase Young's Modulus and the stress resulting from a given strain, though the values did drop before increasing after 144 hours of exposure [16]. The makeup of the

plastic causes a transition period before regaining and increasing in strength. Most importantly, it is possible to derive an analytical model for changes in a plastic's Yield Tensile Strength (YTS) after exposure to hard UV radiation and various temperatures, -50 °C to 90 °C, as a function of time, temperature, and strain rate [17]. While beyond this research's scope, a similar relationship is likely to exist for ULTEM 9085.

There has been research into finding ways to mitigate the effects of UV radiation on plastics, mostly by adding material that fluoresces, rearranges, or simply blocks the radiation [18]. While important to understanding how plastics interact with UV radiation, these compounds are not included in the COTS UTLEM 9085 investigated in this research. The previous research also discussed how the molecules of the plastic changed with exposure to the vacuum, temperatures, and/or UV . This was not studied in this thesis due to limitations on scope and resources.

For approximating orbital solar conditions, the sun is assumed to be a blackbody at 5,900 K [19]. The emissive power per unit area of a blackbody curve is:

$$E_b = \int_0^\infty \frac{C_1}{\lambda^5[e^{C_2/(\lambda T)} - 1]} \mathrm{d}\lambda = \sigma T^4 \tag{2.1}$$

where C_1 equals 3.742E8 W/m^2, C_2 equals 1.439E4 μm, λ equals wavelength in μm, and σ is the Stefan-Boltzmann constant of 5.67E-8 $W/(m^2K^4)$. Total emissive energy for a given blackbody must equal the Stefan–Boltzmann law [15]. Integrating up to a specific wavelength and dividing by the total emissive energy gives the fraction of energy emitted up to that wavelength. The energy between two wavelengths can be found by the difference of two of these integrals:

$$F_{\lambda_1 \to \lambda_2} = \frac{\int_0^{\lambda_2} E_{\lambda,b}\, \mathrm{d}\lambda - \int_0^{\lambda_1} E_{\lambda,b}\, \mathrm{d}\lambda}{\sigma T^4} = F_{0 \to \lambda_2} - F_{0 \to \lambda_1} \tag{2.2}$$

where F is the fraction of the area under the emissive curve up to the wavelength in question. This allows calculation of the energy emitted between any two wavelengths [19]. With the sun's total emissivity at LEO being approximately 1353 W/m^2 [15], integrating and subtracting the fractions for 0 μm and 0.4 μm results in in a total of 167.6 W/m^2 at wavelengths below visible.

For this experiment, a Xenon (Xe) arc lamp is used to simulate the UV output of the sun. While Xe bulbs produce little to no energy at very low and very high wavelengths, the sun produces little energy over these same wavelengths as well. The bulbs produce enough energy in the UV to Infared (IR) wavelengths to be an acceptable substitute [20]. Further, the short distance from the bulb to the samples means the amount of UV reaching them will be much higher than if they were at LEO, allowing more exposure in a short time frame.

2.3 Topology Optimization

Topology optimization is the minimization of a structure's mass while still having it meet a set of loads and boundary conditions. Its advantage lies in being unrestricted to a preset style, rather allowing the loads and boundary conditions to inform the final shape [21]. This method is very FDM friendly because most shapes can be created by an FDM printer with minimal changes compared to other methods. This means a plausible design for a 3-D printed beam can be optimized even with little information about the printer to be used.

The actual optimization algorithm is based on the power-law approach, also called the Solid Isotropic Material with Penalization (SIMP) method. SIMP minimizes a compliance matrix for each element, which is the inverse of the stiffness matrix and a function of whatever design parameter is of interest. The ultimate goal is to keep the global stiffness as large as possible given a requested volume reduction. While

possible to maximize the stiffness rather than minimize the compliance, it is harder for a computer to maximize a value compared to minimizing one. The optimization equation and constraints are:

$$c(\mathbf{x}) = \mathbf{U}^T\mathbf{K}\mathbf{U} = \sum_{e=1}^{N_{el}} (x_e)^p \mathbf{u}_e^T \mathbf{k}_0 \mathbf{u}_e \tag{2.3a}$$

$$\text{subject to} : \frac{V(x)}{V_0} = f, \mathbf{K}\mathbf{U} = \mathbf{F}, 0 < x_{min} \leq x \leq 1 \tag{2.3b}$$

where $\mathbf{U}$ is the global displacement vector, $\mathbf{K}$ is the global stiffness matrix, $\mathbf{F}$ is the global force vector, $\mathbf{u}_e$ is the element displacement vector, $\mathbf{k}_0$ is the element stiffness matrix, N_{el} is the number of elements under consideration, p is the penalization power (3 in the standard SIMP algorithm used here), $V(x)$ is the current volume, V_0 is the original volume, f is the volume fraction being used, x is the design variable vector, and x_{min} is a vector of a minimum non-zero of the design variable. Here, x is a vector consisting of the normalized densities of each element, the parameter used in standard SIMP analysis. The relation between the density of an element and its stiffness matrix is:

$$\bar{K}(\rho) = \rho^p K \tag{2.4}$$

where K is the original stiffness matrix, ρ is the normalized density, and $\bar{K}$ is the penalized stiffness matrix [22]. The penalized local stiffness matrix is used to build the global stiffness matrix in Equ. 2.3a. The penalization power is included to significantly reduce the contribution of low density elements to the overall stiffness [23]. This algorithm assumes that the material properties are constant across all elements. While this may not be true for an FDM-printed part due to the air gaps between the fibers, it is robust enough for this analysis.

While x could be any material property of the topology, using density and tying

it to stiffness is simple and easy to conceptualize, less material means lower material strength. There are other approaches to SIMP, one tying the penalization power to Poisson's ratio and using strain energy as the x variable. The density is still varied but dependent on the strain energy resulting from plane stresses or plane strains rather than from the stiffness directly [24]. While good for small displacement linear elastic theory, this methodology is meant for isotropic materials that have more predictable behavior. Since a complete model of printed ULTEM 9085's structural behavior does not exist and this research's optimization is preliminary, there are few reasons reason to use a more complex method.

III. Methodology

3.1 Orbital Exposure Testing

3.1.1 UV Exposure

The Small Vacuum Chamber (SVC) is a hollow cylinder 60 centimeters (cm) in diameter and 62 cm deep with several access ports. All but two ports were sealed for Ultraviolet (UV) exposure testing, one fitted to allow thermocouple access and one with a quartz porthole. The Newport UV source was mounted outside the SVC, securely attached to heavy worktable to reduce unexpected movement. The source's light was directed through the porthole to the interior of the SVC. The quartz pane was engineered to filter out wavelengths above 4 micrometers (μm), and with the Xenon (Xe) bulb not emitting wavelengths below 0.2 μm, it was necessary to make sure the setup still approximated the sun's behavior well. Resolving for between 0.2 μm and 0.4 μm using Equ. 2.2 resulted in 165.5 W/m^2, a difference of 1.27% compared to the value found in Section 2.2.2 (167.6 W/m^2). This small loss of energy was acceptable in light of needing to expose the test samples to several Sols worth of UV radiation. A cover was also placed over the gap between the source and the porthole. This both reduced unwanted wavelengths entering the chamber and allowed personnel to approach the chamber without protective equipment. In addition, reflective material was attached to the inside of the SVC and the cover to keep the cover from melting by reflecting most of the light away.

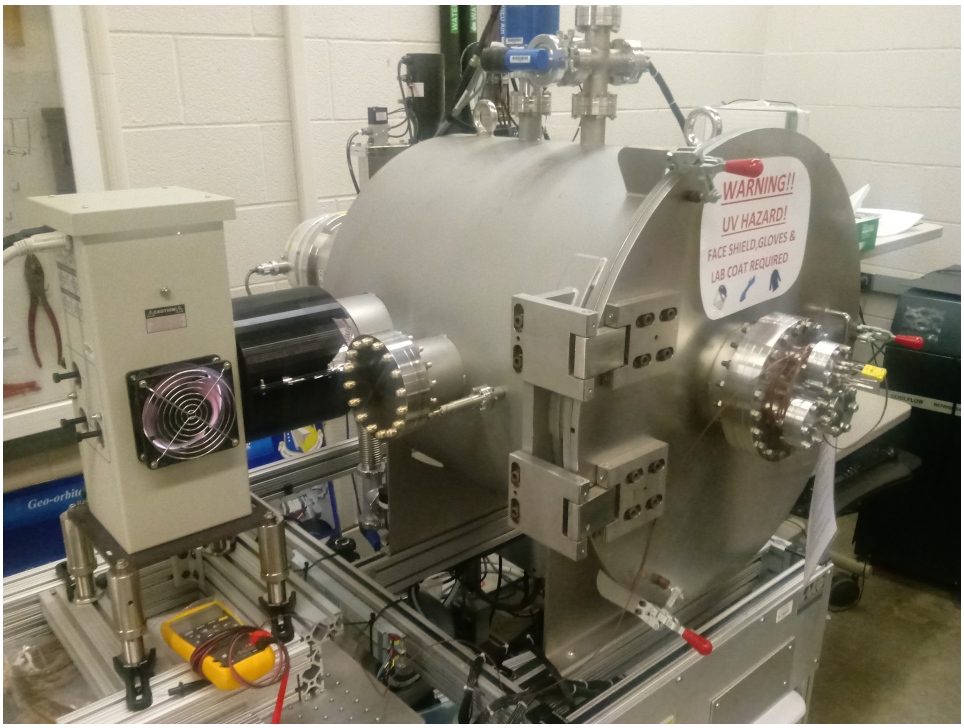

Figure 3.1. The SVC with the UV source mounted on the left and the UV Xenon bulb on.

To calculate exactly how many Sols worth of exposure the samples would be receiving, a Thorlabs Thermal Power Sensor was used to measure the wattage across its 25 millimeters (mm) diameter aperture at the same distance from the bulb as the samples. Because the Power Sensor could not differentiate the wavelengths it was measuring, the resulting wattage was compared to the total wattage that would be expected from the sun. Dividing the solar irradiance at Low Earth Orbit (LEO) (1353 W/m^2) by the sensor's area, the Power Sensor would measure 0.664 Watt (W) at 1 Sols of exposure inside the chamber.

The source's bulb was a Newport 1,000 W Xe bulb. A higher wattage bulb was selected to expose the samples to more than 1 Sol of UV radiation over the duration of time available for experimentation. Xe bulbs can simulate solar UV exposure because of doppler and collisional broadening. With the bulb above 5,000 Kelvin (K) during operation and using reflectors to maximize the energy leaving the source, the photons

from the ionized Xe particles varied in energy by the time they entered the SVC. Combined with the Xe gas being very dense and energized in the bulbs, there is 'smearing' of the emitted wavelengths. Comparing a normalized 5,900 K blackbody curve and a normalized emissivity curve provided by the bulb's manufacturer [20], the sun and the bulb are similar in the energy emitted at UV and visible wavelengths [19]. However, there are numerous spikes in emissivity in the Infared (IR) wavelengths.

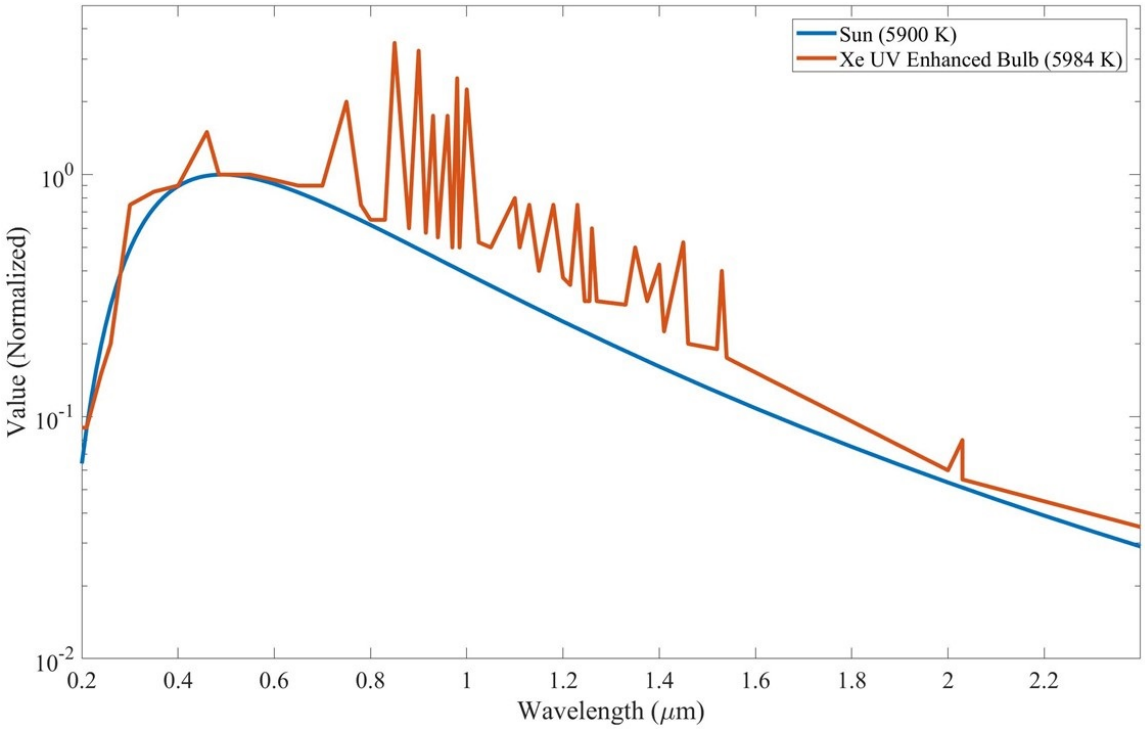

Figure 3.2. The normalized irradiance curves of the sun and the bulb. The bulb does not emit energy below 0.2 μm

The bulbs had an expected operational life of 1,000 hours, so several bulbs were used during the experiment. Each bulb was used for approximately 950 to 980 hours to ensure they did not fail or burn out out unexpectedly. Upon initial installation and before disposal, each bulb's maximum intensity and its position of maximum intensity was measured with the Power Sensor to quantify any changes that occurred during its operation. While the mirrors inside the source were aligned to center the light among the samples, it was found that the light would drift during exposure.

Any changes in solar exposure due to changes in the source's mirrors or the bulb itself were assumed to be linear and the drop off in UV exposure was assumed to fit a Gaussian curve relating intensity to radial position.

The samples inside the SVC were only exposed to the UV once the SVC's internal pressure was reduced to 0.1 milliTorr, and the bulb was turned off for at least 12 hours before the SVC was repressurized. During normal operations, the SVC's internal pressure, internal temperature, the source's power consumption, current, voltage and operating time were recorded daily.

3.1.2 ULTEM 9085 Samples

ASTM D638-14 was selected as the basis for tensile testing the ULTEM 9085, though the standard was not written with Fused Deposition Modeling (FDM)-printed parts in mind [25]. However, due to the size of the SVC and the area of usable UV exposure, it was necessary to reduce the testing dogbones to 1/4th their standard size, resulting in a thickness of 0.8255 mm, neck length of 8.89 mm, and neck width of 1.5875 mm (Fig. 3.3). While increasing the possibility of errors due to the size reduction, it was more important to have data to work with. The dogbones were printed in sets of 8 using the Stratasys 450mc FDM printer, with the print direction parallel to the 'T' direction.

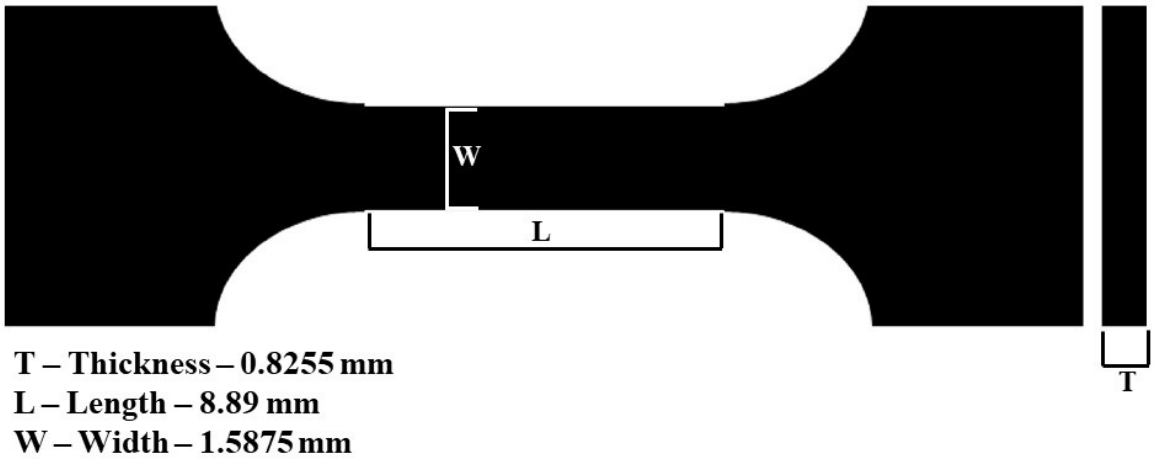

T – Thickness – 0.8255 mm
L – Length – 8.89 mm
W – Width – 1.5875 mm

Figure 3.3. The key dimensions of the 1/4th scale dogbones used in testing.

Figure 3.4. One of the FDM printed ULTEM 9085 dogbone sets.

The sets were arranged in a circular pattern on an aluminum mounting plate to maximize exposure to the UV radiation as shown in Fig. 3.5. Unfortunately, it was discovered that the set at the center of the circle was destroyed due to high temperatures which exceeded the glass transition point of the ULTEM 9085. Subsequent testing showed the samples could only withstand approximately 3.5 Sols of incident radiation before deforming.

On the reverse side of the plate, 6 additional sets were mounted. These were not exposed directly to UV radiation, only to the vacuum and increased temperature due to radiative heating inside the SVC. A thermocouple was also mounted on the reverse side, it was connected to the appropriate port on the front of the SVC to allow a digital readout to display the temperature of the plate. The plate the sets were attached to was mounted in a frame which in turn was placed in the SVC. The frame was designed to only fit one way to reduce misalignment.

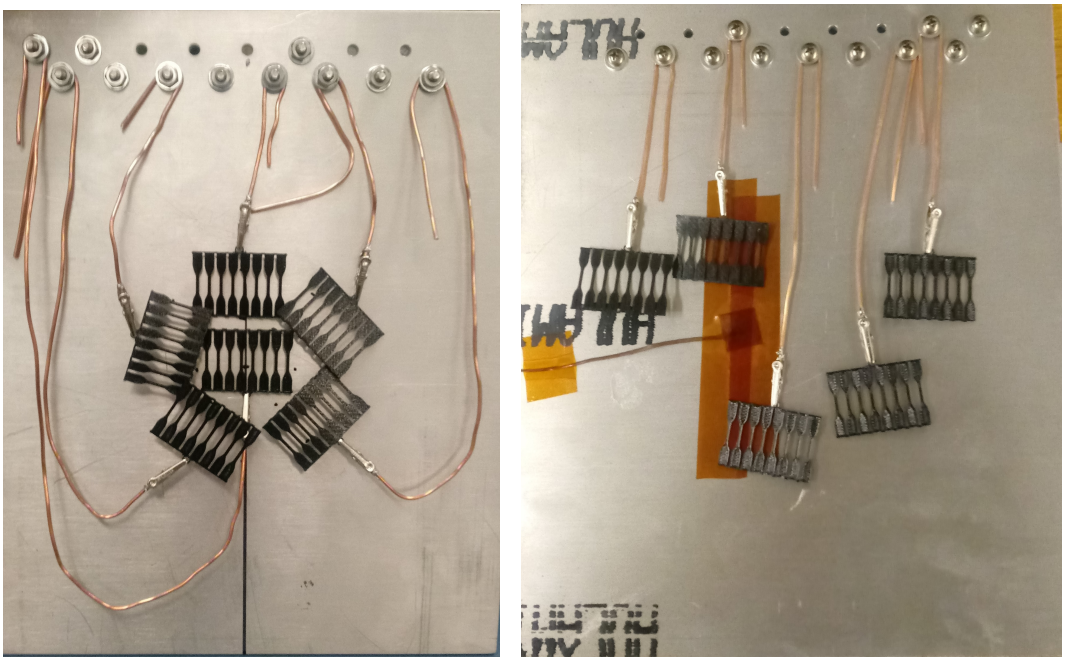

Figure 3.5. The initial configurations of the samples mounted on the plate inside the SVC, with (left) the samples on the UV exposure face and (right) the samples on the opposing (dark) face.

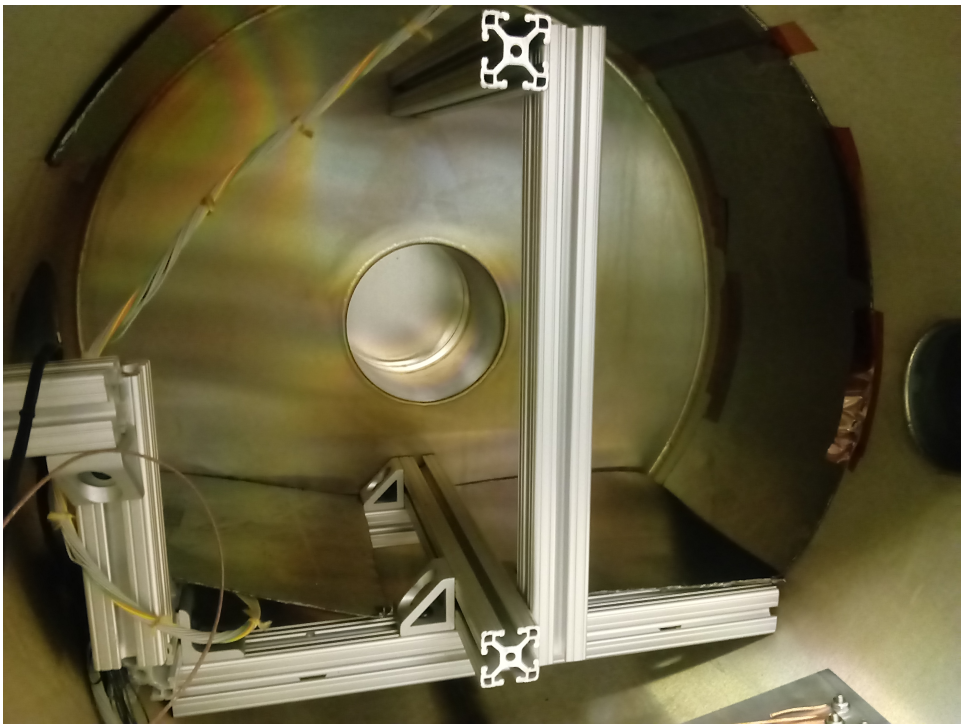

Figure 3.6. The mounting frame inside the SVC without the sample plate.

Each time a bulb was replaced, two sets were removed, one from each side of the plate. These sets were placed in a dry box to to minimize the amount of water and contaminants they would absorb from the atmosphere until they could undergo tensile testing. This was repeated 4 times, resulting in a total of 8 sets of varying amounts of exposure to UV, vacuum, and elevated temperature conditions, along with a single control group. The time each set spent in the SVC with the bulb on was also recorded.

To find the effective time at 1 Sol for a set exposed to UV radiation, the average wattage the set was exposed to was divided by the 1 Sol wattage of 0.664 W. This value was then multiplied by the time it spent in the SVC. To further account for real orbital conditions, the time spent at 1 Sol was assumed to be the daylight time of the International Space Station (ISS)'s orbit. The ISS has an apogee altitude of 410 kilometers (km), a perigee altitude of 408 km, and an inclination of 51.64°. Using

these values and assuming the Earth's radius is 6,371 km, the fraction of the time spent in eclipse was found:

$$E = (\frac{\gamma}{180})(\frac{R_E + H}{a}) \tag{3.1}$$

where E is eclipse fraction time, γ is the Earth's angular radius in degrees at the point under calculation, R_E is the radius of the Earth, and H is height of the point under calculation [26]. The average of the eclipse fractions at apogee and perigee was found to be 0.3889, or 0.6111 for the fraction of time in sunlight. The time spent at 1 Sol was divided by 0.611 to find the total time spent on orbit at 1 Sol for each set exposed to UV radiation. No adjustments were made to approximate how the UTLEM 9085 would behave transitioning from sunlight to eclipse conditions.

3.1.3 Tensile Testing

After being removed from the dry box, the individual dogbones from each set were separated and photographed with a Zeiss Discovery V.12 SteREO optical microscope. Reference photographs of each dogbone's neck was taken at 10x magnification. The exact width and thickness of each dogbone was also recorded with a pair of calipers despite all the dogbones being printed from the same file with the same machine. The resolution of the Fortus printer was not sufficient to produce identical parts at the size required. Knowing the exact cross-sectional area of each sample allowed for the most accurate engineering stress and engineering strain calculations. This procedure was also done for the control set.

The samples were subjected to axial tensile loading using Air Force Institute of Technology (AFIT)'s MTS 250 Tytron Microtester (MTS) shown in figure 3.7. Each dogbone was aligned with the center of the jaws and secured using pliers to tighten the jaws shown in Figure 3.8). Each sample was subjected to a loading rate of 5.08 mm/min per ASTM D638-14 [25], with the MTS using a 250 Newton (N) loading cell. The MTS was programmed to stop deformation once the dogbone fractured.

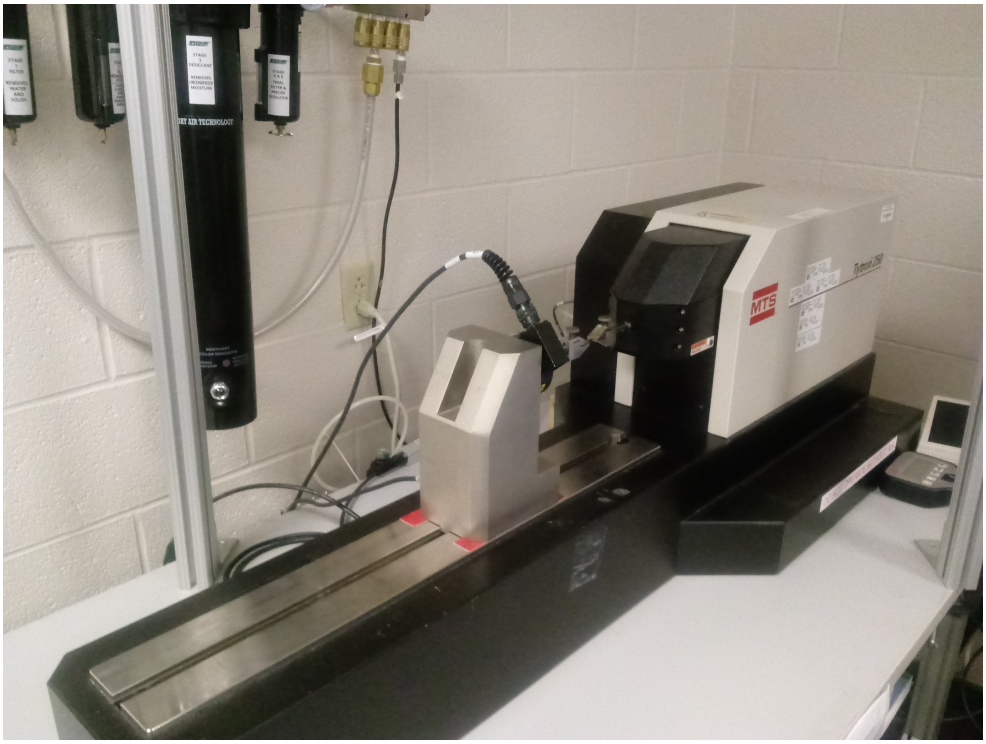

Figure 3.7. The MTS Microtester used to deform each sample after exposure.

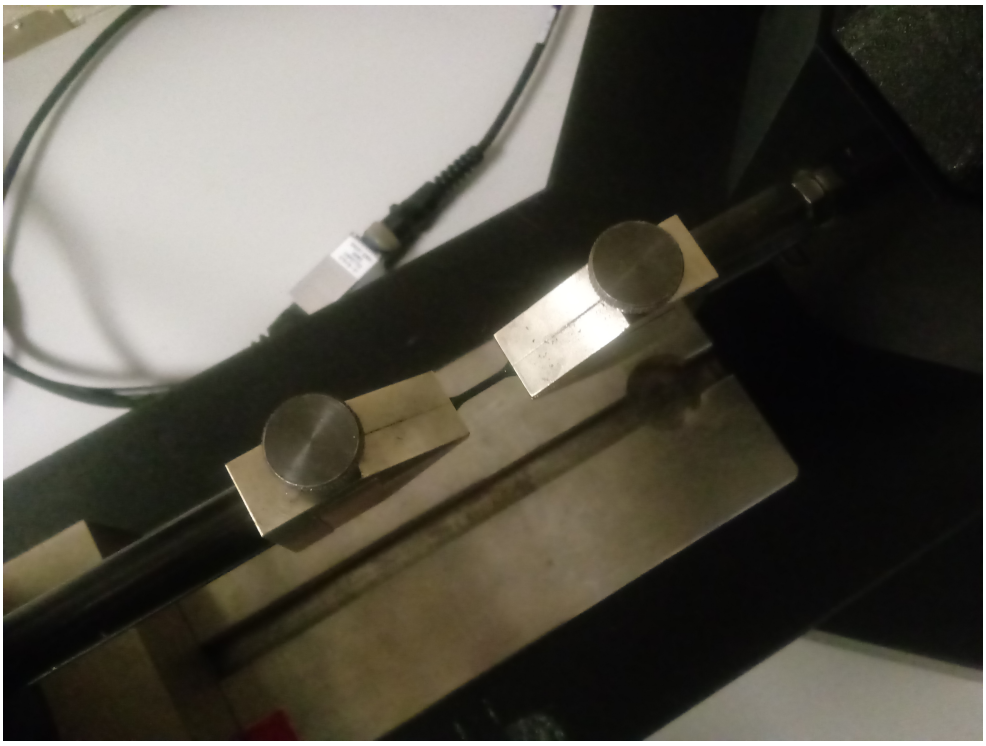

Figure 3.8. A sample mounted in the MTS before testing.

The MTS recorded time to fracture, displacement, and applied force in seconds, mm and N respectively. This information was exported as separate text file for each dogbone. This data was then saved into Microsoft Excel for easy manipulation. Each dogbone was then rephotographed, focusing on the fractured ends and the now visible cross-sectional area. Using the Ziess ZEN Core software and the calipers, the new thickness and width values of the areas were found. ZEN Core allows a pixel count to be translated to a distance based on the lens type, zoom, and focus values each photo was taken at. If the dogbone fractured in the neck, the ZEN Core was used for measuring. If the dogbone fractured at the root, the calipers were used instead. These new dimensions were also included in the Excel files.

This data was imported into MATLAB and the resulting stress-strain relation for each dogbone built. These relations were then used to determine the Ultimate Tensile Strength (UTS), Yield Tensile Strength (YTS), Young's modulus, Poisson's ratio, and Fracture Strain. For consistency, the same algorithm was used for finding each characteristic. The UTS was the largest stress value experienced by a given dogbone. To find Young's modulus, an 1st degree equation for the linear part of each stress-strain curve was approximated using the least-squares method (Equs. 3.2a and 3.2b). A 1st degree approximation was used to produce a single, constant slope value. The slope of said approximation was found using the 1,000 data points on either side of the point where the strain was 0.0015. This reduced the influence of errors caused by errors when the loading force was close to 0 N. This minimized the influence of error while capturing as little of the non-linear stress-strain relation as possible. The resulting slope of this line was recorded as Young's modulus.

$$\begin{bmatrix} 1 & x_1 \\ 1 & x_2 \\ . & . \\ 1 & x_n \end{bmatrix} * \begin{bmatrix} a_1 \\ a_2 \end{bmatrix} = \begin{bmatrix} y_1 \\ y_2 \\ . \\ y_n \end{bmatrix} \tag{3.2a}$$

$$y = a_1 + a_2 x \tag{3.2b}$$

When finding the YTS, it was assumed the YTS was the stress where the slope of the stress-strain curve equaled 90% the value of Young's Modulus. A 7th degree polynomial least-squared estimation was applied to the entire stress-strain curve (Equs. 3.3a and 3.3b), and its slope was calculated using the derivative of the 7th degree polynomial (Equ. 3.4). The 7th degree approximation provided the most accurate estimation of the stress-strain curve up to the UTS. This value was compared to the respective Young's Modulus to find the YTS.

$$\begin{bmatrix} 1 & x_1 & x_1^2 & . & x_1^7 \\ 1 & x_2 & x_2^2 & . & x_2^7 \\ . & . & . & . & \\ 1 & x_n & x_n^2 & . & x_n^7 \end{bmatrix} * \begin{bmatrix} a_1 \\ a_2 \\ . \\ a_8 \end{bmatrix} = \begin{bmatrix} y_1 \\ y_2 \\ . \\ y_n \end{bmatrix} \tag{3.3a}$$

$$y = a_1 + a_2 x ... + a_8 x^7 \tag{3.3b}$$

$$y = a_2 + 2a_3 x ... + 7a_8 x^6 \tag{3.4}$$

Poisson's ratio was calculated by dividing the negative of the average of the change in the width and thickness by the change in length of each dogbone (Equ. 3.5).

$$\nu = -\frac{\frac{\Delta T + \Delta W}{2}}{\Delta L} \tag{3.5}$$

This is not the normally accepted way to calculate Poisson's ratio. Normally one must start with a square cross-section and divide the change in the thickness and/or width by the change in length (Equ. 3.6), assuming the change in thickness and width are the same. The approximation had to be used due to the design of the dogbones.

$$\nu = -\frac{\Delta L'}{\Delta L} \tag{3.6}$$

The Fracture Strain was the time to fracture times the rate of displacement divided by the original neck length.

3.2 Topology Optimization

3.2.1 Initial Design and Hyperworks Optimization

When designing the beam that would be printed by AFIT's microgravity vacuum 3-D printer, the parameters were based on the capabilities of the Lulzbot TAZ-6 printer used in previous analysis of a vacuum 3-D printer. While not beyond the initial stages of development, the printer nozzle will be on a 6-axis jointed articulating arm similar to the DoBot [7] [27]. The initial beam was assumed to be a solid cylinder of ULTEM 9085 1 meter (m) long and 24 cm in diameter. The cylinder would be printed along its length so the initial footprint would fit inside the TAZ-6's build environment [28]. Since the proposed printer design allows the printer to travel along the printing direction, the beam can be as long as it needs to. The 1 m length was selected for simplicity.

Once the initial beam was designed, it became necessary to determine how much shear stress the beam could withstand. The physical parameters of the ULTEM 9085 were pulled from previous research by Wilburn into printing methods of ULTEM 9085. His research found that the structural characteristics of ULTEM 9085 varied dramatically based on the printing direction of the ULTEM 9085 and the printing temperature. Since Wilburn's thermal analysis was done on samples printed in only one direction, some extrapolation of his data was needed before it could be used for this analysis. While it would have been understandable to use the structural results from this research, the samples tested by Wilburn were larger and more representative of actual parts that would be made with ULTEM 9085. His data was also more thorough, a necessity since this optimization would require more than axial deformation results.

It was decided to use Wilburn's thermal results at 170 °C, a UTS of 36 MegaPascals (MPa) and a Young's Modulus of 987 MPa. Wilburn also found the UTS , YTS , and Young's Modulus for the three printing directions (Table 3.1 and Fig. 3.9) [3].

Table 3.1. Structural Characteristics For Each Printing Direction (Wilburn) (MPa).

Print Direction	UTS	YTS	Young's Modulus
XY	**59**	**30**	**1030**
YX	**87**	**37**	**1530**
ZX	**44**	**28**	**1030**

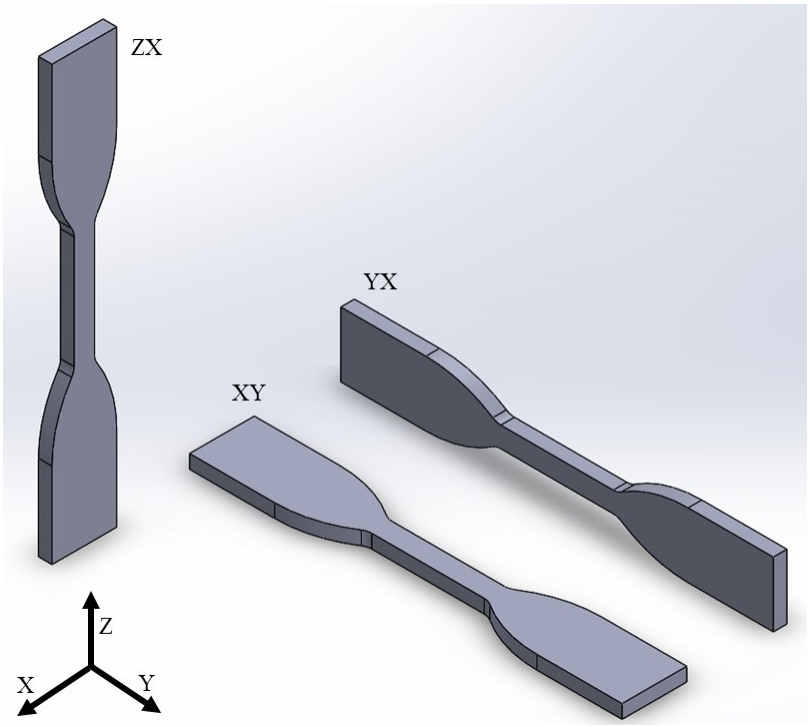

Figure 3.9. The printing directions specified by Wilburn. The print direction was positive Z.

It was assumed that the structural characteristics regardless of print direction would be equally affected by the build temperature, reducing the UTS and YTS linearly. Since the build temperature testing was done on samples printed in the ZX direction, that UTS was assumed to the UTS in the axial direction for this optimization. The axial YTS was assumed to be 23 MPa, the same YTS/UTS ratio as the baseline testing. The same reduction was also done for the XY and YX printing directions (Table 3.2). Poisson's ratio was assumed to be 0.115 for all directions, derived from the control group of the current analysis.

Table 3.2. Structural Characteristics For Each Printing Direction (Adjusted) (MPa)

Print Direction	UTS	YTS	Young's Modulus
XY	**48**	**24**	**987**
YX	**71**	**30**	**1466**
ZX	**36**	**23**	**987**

With the design and structural characteristics of the beam known, the maximum allowable shear stress could be found. It was assumed a single shear load was applied at the free end of the solid cylinder and the structural characteristics used were the adjusted XY values. Since the force is being applied perpendicular to the build direction, the worst case structural characteristics were used. Rewriting the pure shear equation calculates the shear force that will produce the YTS with a Factor of Safety (FoS) of 2 (12.14 MPa) (Equ. 3.7). These shear forces were assumed to not cause any axial deformation.

$$V = \frac{\tau I t}{Q} \tag{3.7a}$$

$$Q = \frac{2r^3}{3} \tag{3.7b}$$

$$I = \frac{\pi r^4}{4} \tag{3.7c}$$

This lead to a value of 560 kiloNewton (kN) as the maximum allowable shear force. However, the design of the vacuum 3-D printer will clamp the printed beam at 4 points, so the maximum shear force was divided by 4 and applied at each attachment point evenly, 140 kN at each point. While this would change that resulting maximum shear stress, Wilburn's research shows that the actual structure will be stronger than assumed in the above calculations due to the interaction of the XY and YX printing directions. Since the exact interaction of the print orientations is unknown, using the minimum mechanical strength was the conservative choice.

To account for flexibility in the design of the printer, 9 configurations of the 4 loads were analyzed with Hyperworks (Fig. 3.10), resulting in 9 topologies. For the optimization, a circle of 2-D quadratic elements was created, totaling 3,360 elements

and 10,228 nodes (Fig. 3.11). The circle was reduced to a radius of 10.8 cm for this analysis, resulting in the final design having a minimum outer thickness of 1.2 cm. Optistruct, Hyperwork's optimization suite, was programmed to assume the elements had a thickness of 1 m and to reduce the volume by 35%, removing more material caused some of the optimized topologies to be two distinct pieces. Hyperworks has the Solid Isotropic Material with Penalization (SIMP) algorithm discussed previously as a default solver, so it was only necessary to specify the volume to reduce and the density as the design variable. All nodes were locked in the Z direction and for all rotation during the analysis. The optimized results can be viewed in Appendix B.

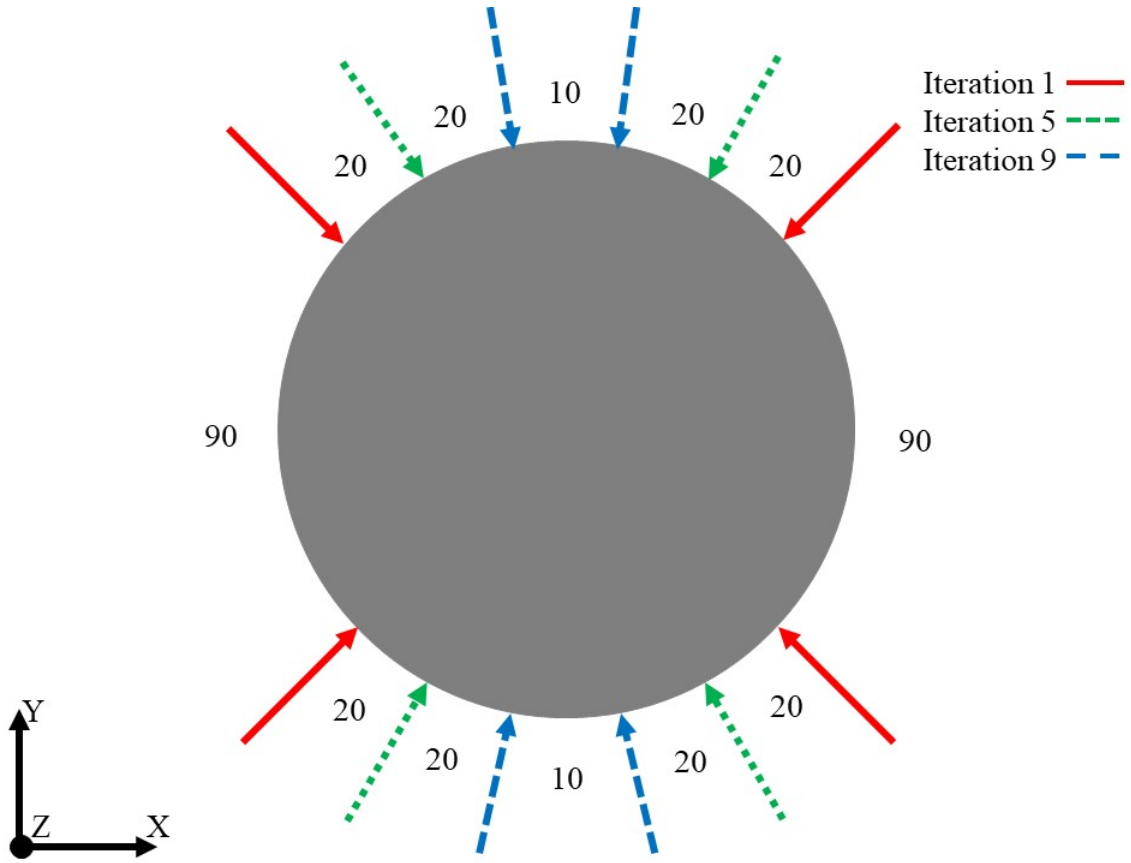

Figure 3.10. The load positions analyzed optimized in Hyperworks, the remainder are positioned equally between the shown loads (degrees).

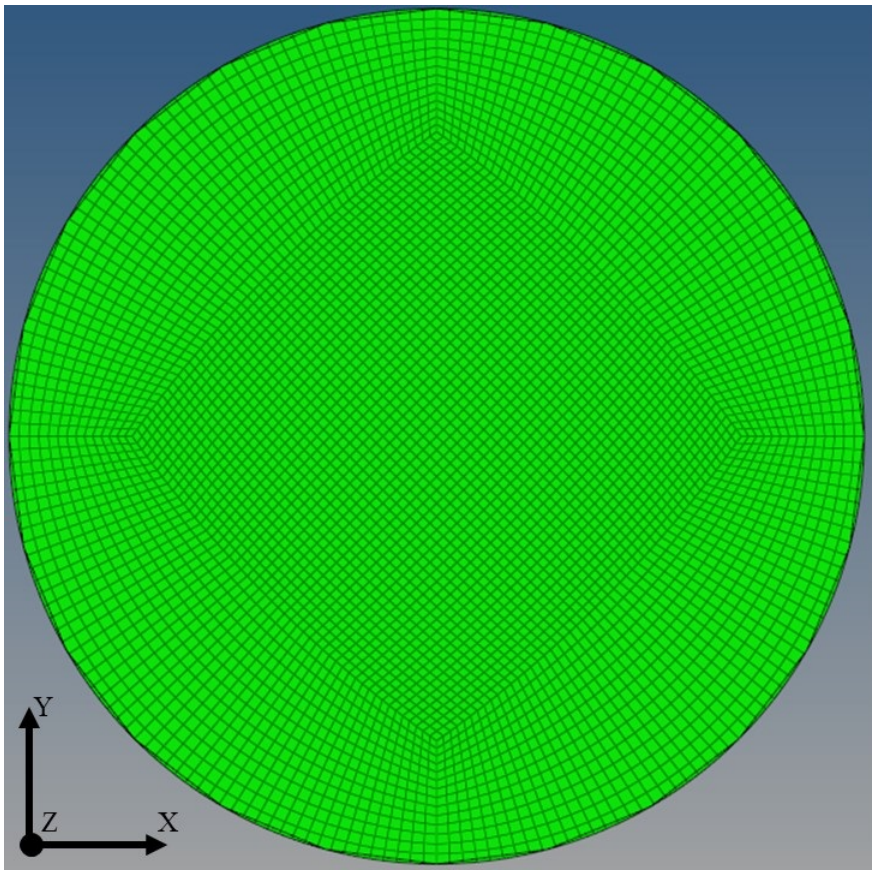

Figure 3.11. The mesh used for optimization in Optistruct.

3.2.2 SolidWorks Analysis and Refinement

Each optimization result was converted into an STL file and imported into Solidworks. The files were manually compared to see where material was most common and a new beam model designed, which included the outer shell left off of the Hyperworks model. This model was then used in Solidworks to find the maximum bending moment the beam could withstand. The resulting shear stress and Von Mises stress for each iteration were saved and averaged.

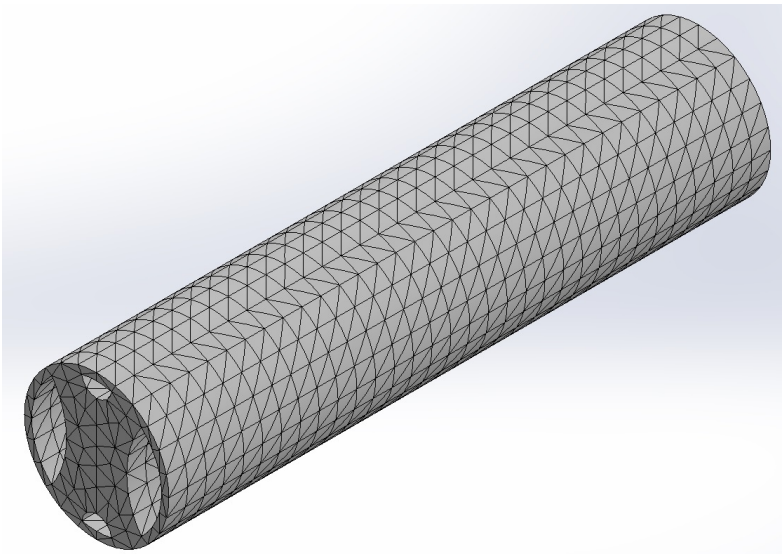

Figure 3.12. The mesh of the final beam design.

To determine the allowable axial stress, the resulting axial stress from the average shear stress and Von Mises stress was computed, resulting in 13.83 MPa (Equ. 3.8). This assumes that σ_{11}, σ_{22} , σ_{12}, σ_{23}, and σ_{31} equal 0 since there are no forces creating stresses in those directions. Again, while the actual beam would be able to withstand more stress due to its anisotropicity, designing to a worst-case scenario was best with the number of assumptions being made.

$$\sigma_v = \sqrt{\frac{(\sigma_{11} - \sigma_{22})^2 + (\sigma_{22} - \sigma_{33})^2 + (\sigma_{33} - \sigma_{11})^2 + 6(\sigma_{12}^2 + \sigma_{23}^2 + \sigma_{31}^2)}{2}} \tag{3.8}$$

Solidworks was used for this part of the analysis due to Hyperwork's results disagreeing with analytical estimates. The shear stress in Hyperworks was distributed in a way that diverged from the axial stress due to bending equation, y equaling the perpendicular distance from the neutral axis:

$$\sigma_{33} = \frac{My}{I} \tag{3.9}$$

A mesh was created of the optimized beam using Solidwork's default mesh of triangular prism elements, totaling 9,902 elements and 16,863 nodes. A moment was applied to one face and the other face clamped, using the adjusted ZX values and again assuming the shear force did not influence the axial deformation. 10 analysis were done, each one rotating the moment 10° clockwise (Fig. 3.13). An initial analysis showed the moment rotated 90° from the initial orientation produced the most axial stress, so the moment was adjusted until the stress resulting from that moment was 98% of the allowable axial stress, a value of 10 kiloNewton meters (kN-m). Similar to the shear analysis, it was assumed the bending moment caused no shear deformation.

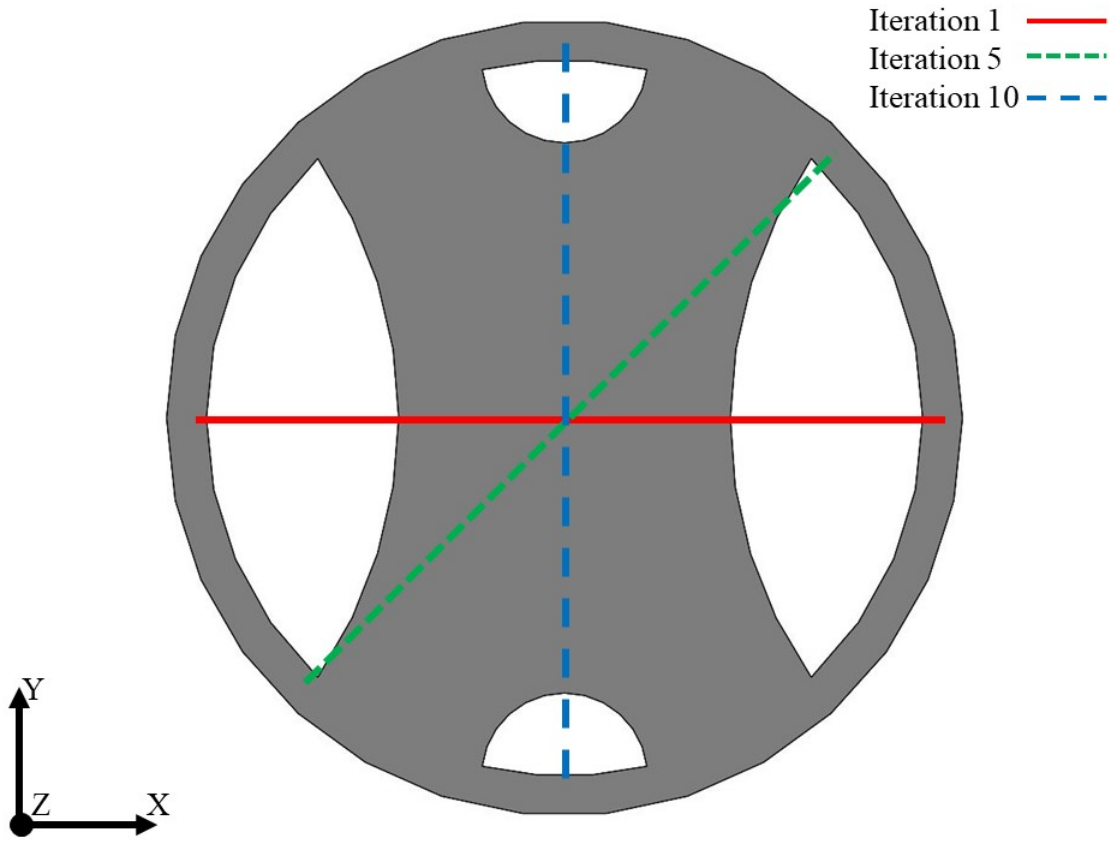

Figure 3.13. The neutral axises of the applied moment, the remainder are positioned equally between the shown axises.

The final result is a beam of printed ULTEM 9085 1 m long with a 12 cm radius that can withstand 4 shear forces of 140 kN applied symmetrically and a moment of 10 kN at one end. This assumes a FoS of 2 and worst case structural characteristics of the ULTEM 9085.

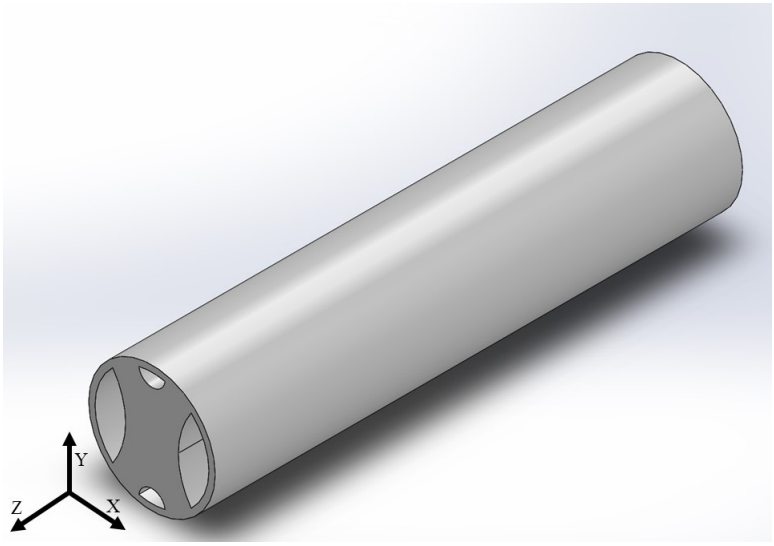

Figure 3.14. The final design of the vacuum printed ULTEM 9085 beam.

IV. Results

4.1 Tensile Testing

It took several months to test 8 sets of dogbones, 4 exposed to Ultraviolet (UV) radiation while in the Small Vacuum Chamber (SVC), 4 with no UV exposure. This required 4 Xe bulbs and 3,730 total hours in the chamber. Two Gaussian curves were modeled for each bulb's UV exposure pattern, one at the start of exposure and one at the end. Any shifts in the point of maximum solar exposure was also accounted for when estimating the change in solar exposure.

The upper limit of 3.5 Sols the dogbones could withstand before melting was discovered accidentally by incorrectly aligning the first bulb before sealing the SVC (Fig. 4.1). The Infared (IR) spikes in the Xenon (Xe) bulbs' emissivity probably helped increase the dogbone's temperatures to the glass transition point. Subsequent bulbs were aligned and measured more thoroughly and the center sample removed to avoid destroying more sets. However, the exposure data for the first bulb was still usable and the surviving sets included in axial testing. ULTEM 9085 on orbit would be exposed to far less IR radiation and not have this problem.

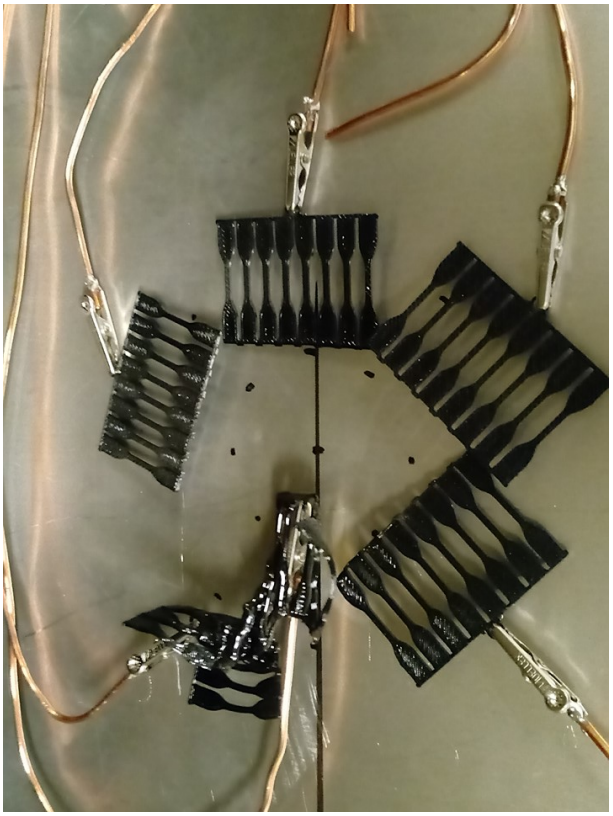

Figure 4.1. Damage to the samples caused by excessive UV exposure.

The time spent on orbit was calculated for each UV set by finding the on-orbit time for each bulb the sets were exposed to and adding the values, with the maximum time on orbit coming out to roughly 1 year and 4 months. With knowing how long each set was exposed to the UV radiation or the vacuum, the mean Young's modulus, Yield Tensile Strength (YTS), Ultimate Tensile Strength (UTS), Poisson's ratio, and Fracture Strain were found for each set. The values were then plotted, against time on orbit for the UV sets and against time in the chamber for the non-UV sets. All data was normalized against the control values for easier comparison when plotting, with error bars derived from the respective Coefficient of Variance (CoV) included as well.

Table 4.1. Exposure time for each exposure condition.

Sample	1 Sol UV Exposure Time (Hrs)	Vacuum Exposure (Hrs)	Average Temperature (°C)
Set 1	0	0	21
UV Sets			
Set 2	226	817	81
Set 6	4,430	2,750	90
Set 4	10,395	1,781	88
Set 8	11,140	3,730	92
non-UV Sets			
Set 3	0	817	81
Set 5	0	1,781	88
Set 7	0	2,750	90
Set 9	0	3,730	92

Table 4.2. The average structural characteristics of the sample sets.

Samples	Young's Modulus (MPa)	YTS (MPa)	UTS (MPa)	Poisson's Ratio	Fracture Strain
Set 1	1,322	30	87	0.115	0.886
UV Sets					
Set 2	1,513	40	101	0.088	0.337
Set 6	1,533	41	102	0.188	0.344
Set 4	1,527	35	102	0.188	0.332
Set 8	1,519	40	101	0.184	0.333
non-UV Sets					
Set 3	1,526	36	96	0.033	0.794
Set 5	1,477	36	94	0.069	1.005
Set 7	1,480	35	91	0.110	0.804
Set 9	1,533	34	91	0.092	0.906

Table 4.3. The CoV of the structural characteristics of the sample sets.

Samples	Young's Modulus	YTS	UTS	Poisson's Ratio	Fracture Strain
Set 1	3.61%	8.86%	4.92%	99.66%	52.52%
UV Sets					
Set 2	4.57%	9.96%	6.31%	104.30%	3.72%
Set 6	2.65%	8.03%	5.90%	43.98%	8.67%
Set 4	2.83%	41.63%	2.73%	34.08%	3.02%
Set 8	2.62%	6.29%	2.87%	24.10%	1.43%
non-UV Sets					
Set 3	2.52%	4.28%	1.83%	84.87%	73.51%
Set 5	2.70%	4.07%	2.38%	92.74%	42.54%
Set 7	2.95%	3.41%	3.26%	78.08%	61.85%
Set 9	1.73%	5.06%	4.11%	88.83%	55.08%

All structural characteristics changed with exposure but the behavior of individual characteristics varied. Young's Modulus increased 15% with and without UV radiation. While appearing independent of UV exposure, the non-UV data is still within an 99.8% confidence interval of the UV data. The error bars on Fig. 4.2 further indicate this, there is a drop in the non-UV average but it never fully separates from the UV data. Conversely, the Fracture Strain not only decreased by 62% with UV exposure, it also became more consistent with an average standard deviation of 5%. The non-UV and UV data are both more than two confidence intervals distant of each other. This correlates well with plastics becoming more brittle with UV exposure.

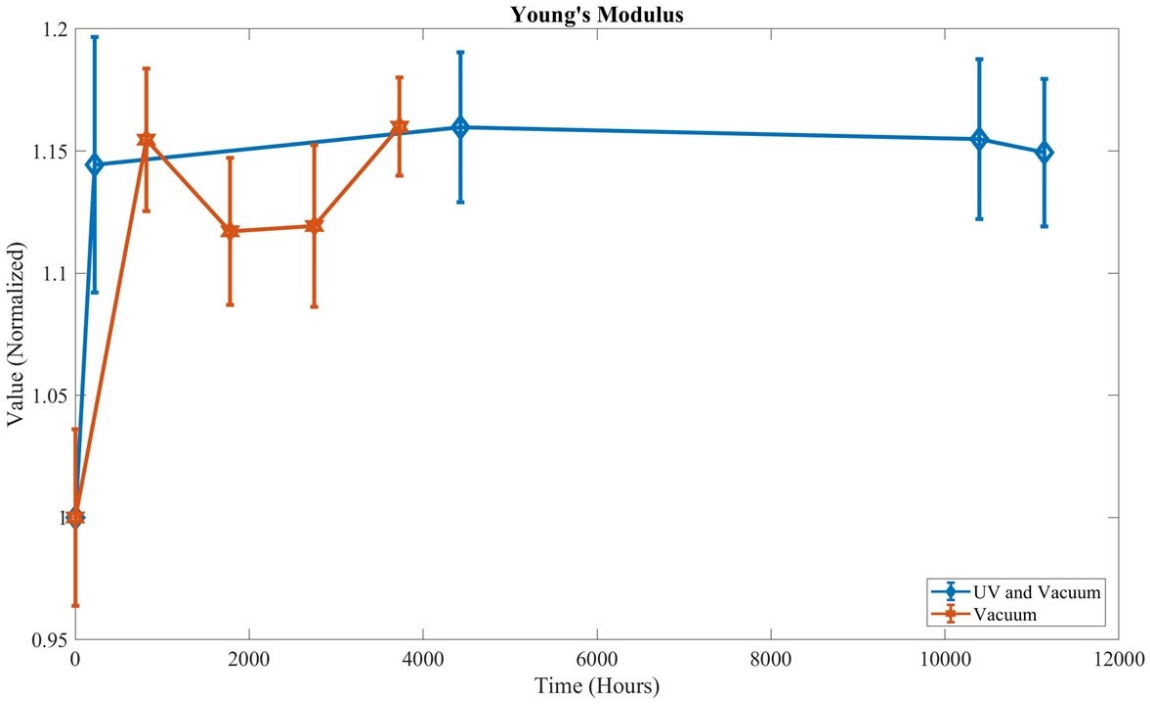

Figure 4.2. Young's Modulus versus Time.

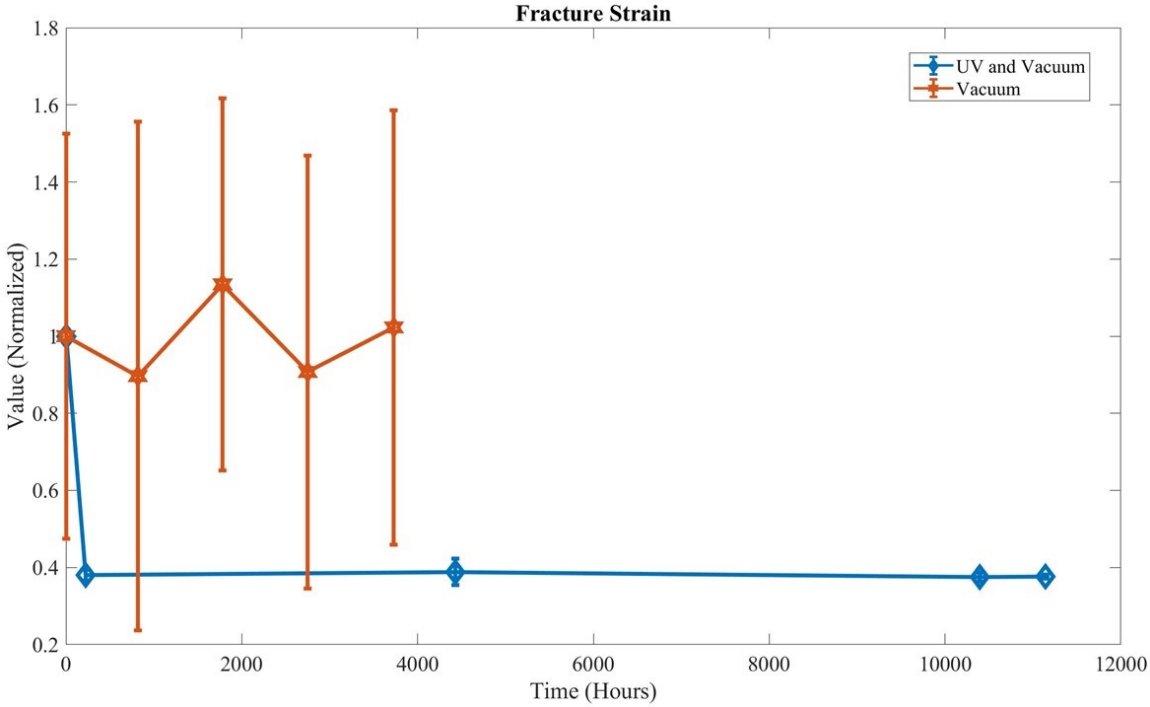

Figure 4.3. Fracture Strain versus Time.

In contrast, there is divergence in the UTS and YTS values, the UV sets increased in value more than the non-UV sets. YTS increased 30% with UV exposure compared to 18% with no UV exposure, 7% and 17% for the UTS respectively. The UTS data sets are outside a 99.9% confidence interval of each other while the non-UV YTS mean is just barely inside the 99.9% confidence interval of the UV data.

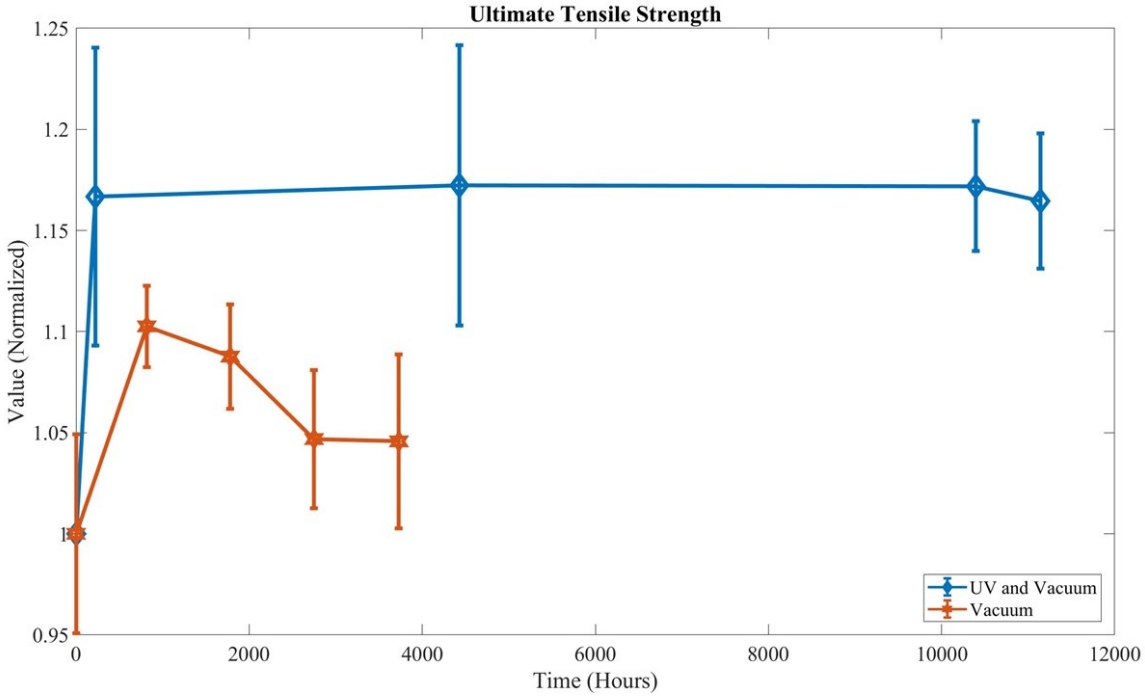

Figure 4.4. Ultimate Tensile Strength versus Time.

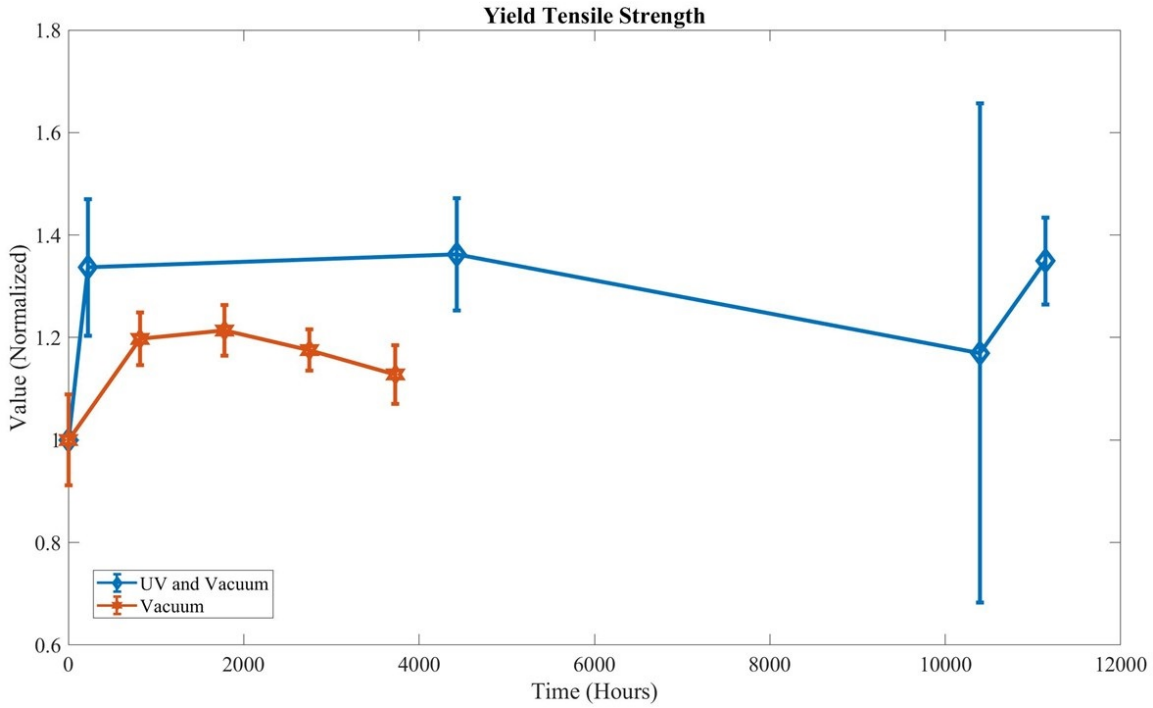

Figure 4.5. Yield Tensile Strength versus Time.

The data for Poisson's ratio is the most divergent, which is unsurprising given how it was calculated. While the Poisson ratio value did increase when exposed to UV radiation, it had the highest CoV of all the UV sets. However, the CoV decreased with UV exposure time, though not as much as with the Fracture Strain. Though the non-UV sets decreased in value, the high CoV makes this observation the least accurate of all the data.

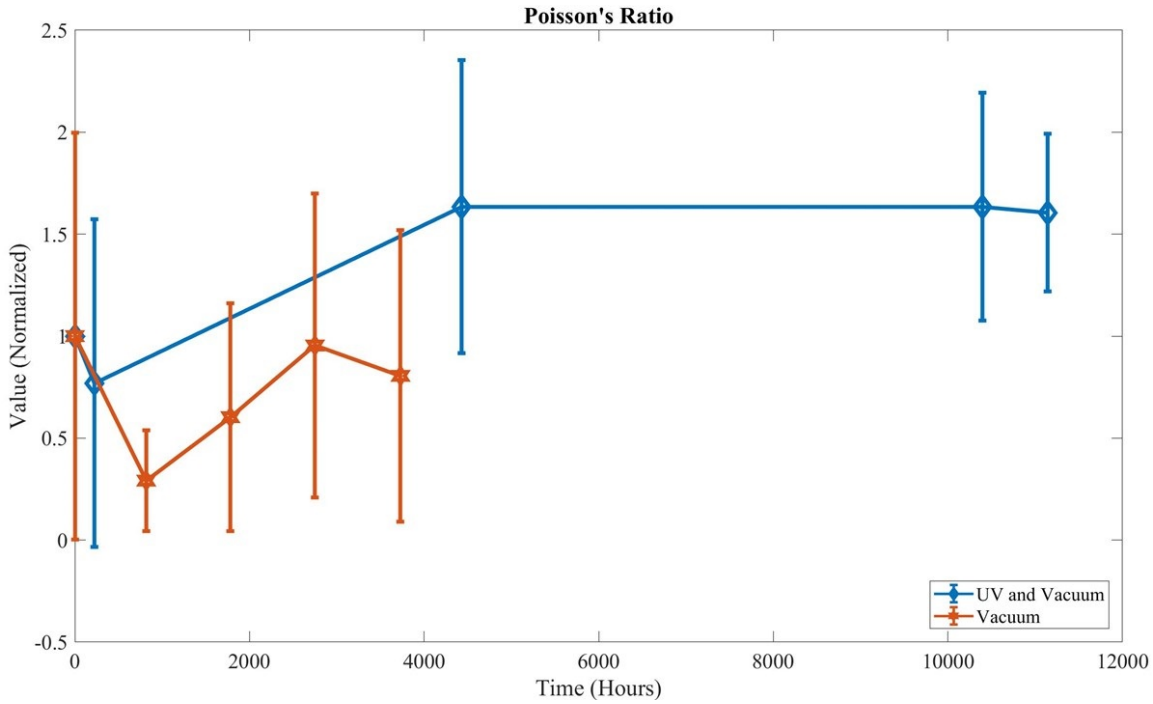

Figure 4.6. Poisson's Ratio versus Time.

YTS and Poisson's ratio have the highest CoVs for both UV and non-UV exposure and are the characteristics that required the most post-processing to calculate. Calculating Poisson's ratio differently and changing the YTS algorithm could reduce these CoVs without requiring a different test set up. While the Fracture Strain has a high CoV as well, it's only for the non-UV samples.

Table 4.4. Average characteristic changes due to exposure.

	High Temp. and Vacuum		**UV, High Temp, and Vacuum**	
	Mean Value	**Standard Deviation**	**Mean Value**	**Standard Deviation**
Young's Modulus	+14%	3%	+15%	3%
YTS	+18%	5%	+30%	20%
UTS	+7%	4%	+17%	4%
Fracture Strain	-1%	59%	-62%	5%

While the non-UV samples are broadly inconsistent in behavior over their exposure time, the UV samples all reach their new values quickly. More importantly, they do not vary much after about 220 hours of exposure. While there still is high variation in the YTS and the Poisson's ratio does decrease before increasing, these can be attributed to post-processing decisions. This shows that not only is there is a limit to the changes UV will cause in ULTEM 9085, there is an exposure amount beyond which the UTLEM 9085 is not further changed by UV radiation. This point is reached in less than two weeks of being on orbit, so every mission using ULTEM 9085 parts will need to account for these changes. This contrasts to the much more unpredictable characteristics of the non-UV data, best shown by the Young's Modulus results. The Young's Modulus UV data has smaller error bars than the non-UV data. Exactly how long this UV-caused change takes cannot be answered here as there is not enough data between Sets 1 and 2.

This is reinforced by examining the data globally in the context of Student's t-distribution. Seeing if the average value of a set is within a given confidence interval of the aggregate of the preceding set(s) shows how consistent the value was over the exposure period. How wide the interval is reflects the variation in the values of the given characteristic. All the characteristics of the UV exposed samples fall within a single confidence interval except for the YTS due to the large error in Set 4. Young's Modulus, YTS , and UTS of the non-UV sets do not fall within a single confidence interval.

The remaining question is what is causing the changes and lower CoV's in the UV sets. Looking at the cross-section of the dogbones after fracturing, the dogbone exposed to UV radiation (Fig. 4.8) has 'scratching' on its lower edge, this is missing on the edges of the control and non-UV dogbones (Figs. 4.7 and 4.9). This is likely surface hardening caused by the UV radiation. Surface hardening only affects a few

Table 4.5. Confidence interval for ULTEM 9085 structural characteristics.

	High Temp, and Vacuum	**UV, High Temp, and Vacuum**
Young's Modulus	80.0%	+99.9%
YTS	+99.9%	+99.9%
UTS	80.0%	+99.9%
Poisson's ratio	98.0%	99.9%
Fracture Strain	90.0%	80.0%

microns from the surface of material, which matches with the scale the below pictures were taken at.

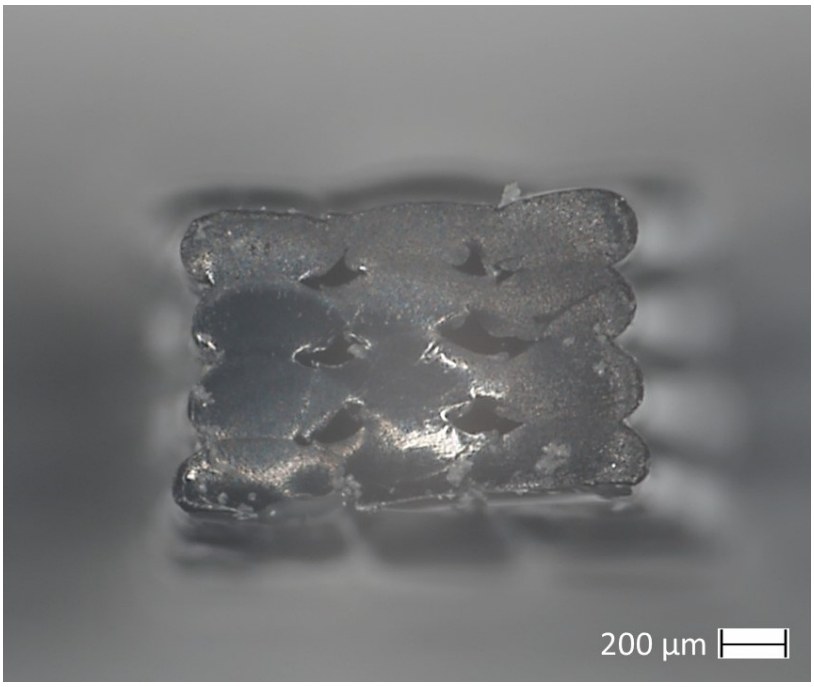

Figure 4.7. The cross-sectional area of a typical control dogbone after testing.

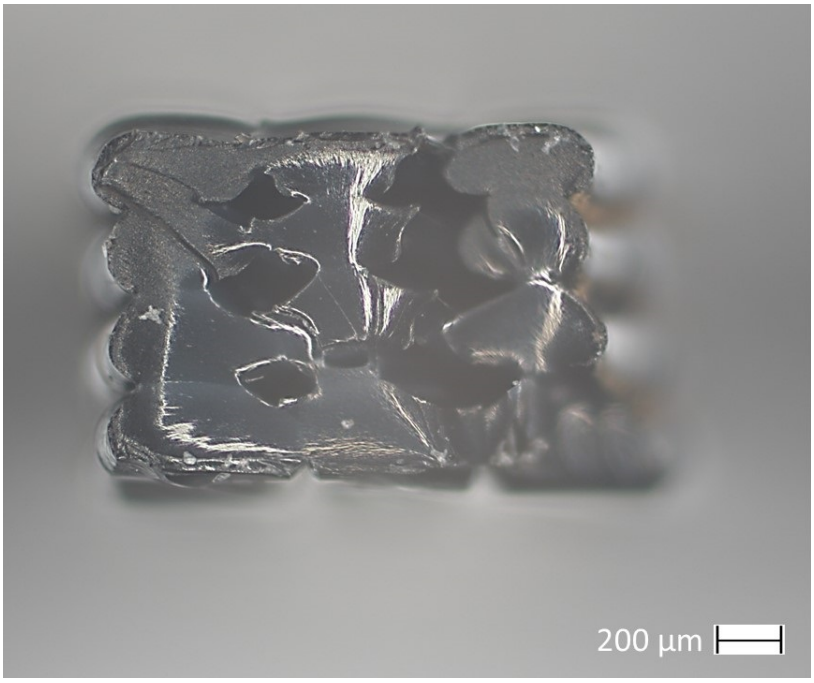

Figure 4.8. The cross-sectional area of a typical dogbone after UV and vacuum exposure and testing. Note the distinct lighter 'scratches' on the center of the lower edge.

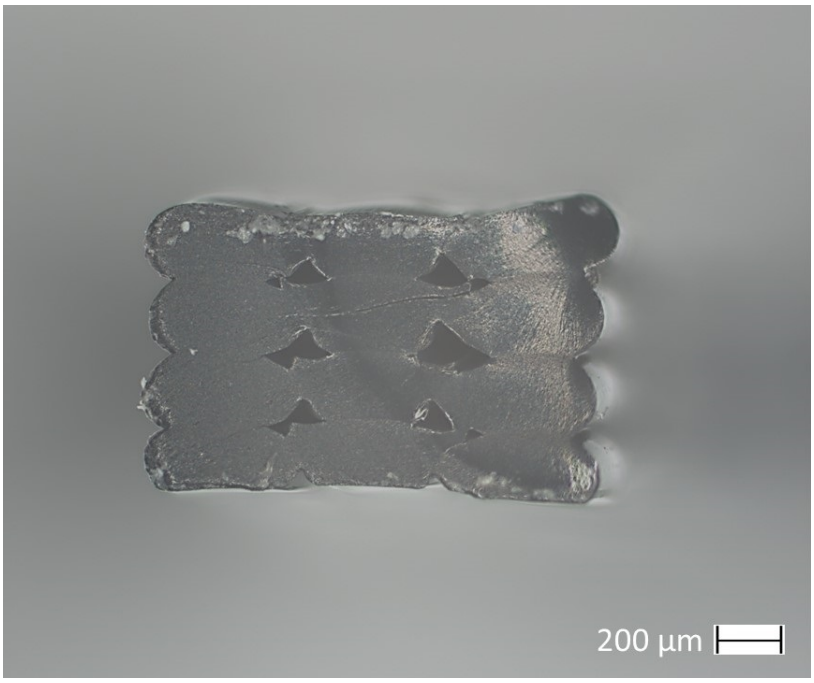

Figure 4.9. The cross-sectional area of a typical dogbone after vacuum exposure and testing.

Any cracks that form in the hardened region during testing would grow quickly, fracturing the UV dogbones faster and more consistently than the non-UV ones. This change must be consistent across all the UV dogbones to reduce the error so dramatically, as seen in Fig. 4.3. These scratches can be seen in other UV dogbone cross-sections as well (Appendix A). Most importantly, the relatively small percentage of the ULTEM 9085's volume being hardened was enough to noticeably increase the overall strength of the dogbones. The dogbones are so small that the percentage of the cross-sectional area affected by the UV radiation is much higher than it would be on a full sized ASTM test sample. This explains the overall CoV reduction for the UV dogbones and the changes in Fracture Strain while also influencing the UTS and the YTS , though the YTS to a lesser degree.

The YTS UV and non-UV data being closer in value seems to be a fault with the UV hardening conclusion. But the YTS is also the characteristic most dependent on calculations, requiring two polynomial approximations in MATLAB. This rigid definition was used to remove human ambiguity when processing the data, but may not apply to every dogbone. Adjusting the definition could completely drop the non-UV data outside the UV confidence interval or make it line up perfectly. The higher CoV in the YTS UV data also indicates there is variation in how the hardened layer affects the underlying raster fill.

This is a problem specific to this experiment due to the dogbone's small size and the resolution of the Fortus printer. There was enough variation in the sizes of the dogbones that a standard pair of calipers could measure the difference. The small size of the dogbones also meant that they spent less time at the production temperature in the Fortus printer. These combined factors not only increased the risk of filament issues, but would be magnified compared to a full size ASTM D638-14 dogbone. A fault in a single filament would reduce the effective area of the dogbone's neck by

6.25%. In contrast, it would take approximately 19 filament failures to cause the same neck area reduction on a full-sized dogbone. It is not known how often the Fortus printer makes an error when printing, but the air gaps visible in the above cross-section pictures show the filaments were not fully melted together. On the other hand, this does mean the stress results are inaccurate because they assume a rectangular neck cross-section. Since the cross-sections shown above are not perfect rectangles and have the filament gaps, the true axial stress of the ULTEM 9085 at fracture is higher than recorded.

Since the surface hardening can only have occurred in the UV sets, something else is causing the changes in the non-UV sets. All the dogbones would be undergoing diffusion due to the vacuum, leaching out compounds leftover from the printing process and water. The UV dogbones would also be at a much higher temperature than the non-UV ones due to the excessive IR exposure. Both of these changes would occur quickly relative to the time spent in the SVC, explaining the lack of significant changes after 200 hours. There's a chance the high CoV for the non-UV sets is to due being re-saturated with the atmosphere several times when the SVC was opened to remove the sets. The higher amount of UV and IR radiation may be helping remove the contaminants and reduce the CoV further in the UV dogbones.

Given the above, it's clear that Fracture Strain is most dependent on the surface hardening and higher temperatures of the UV exposure. Young's Modulus is only dependent on diffusion due to vacuum, as it varies little with the change in temperature and UV exposure. UTS and YTS are mostly dependent on the diffusion, but the surface hardening and higher temperatures do contribute.

4.2 Optimization

The optimization of the beam is less about the result and more about the selected parameters. Because there is no specific hardware designed for the printer that would print this beam, the final design is based on an averaging of several shear loading configurations. Ideally it would withstand any of the loading patterns thanks to the Factor of Safety (FoS). The length was selected to help keep the analysis straightforward rather than derived from a specific mission need. Optimizing a beam for a specific purpose, knowing the satellite's configuration, the printer's specifications, and mission design would result in a more useful model.

The largest obstacle encountered during the analysis is the lack of information needed to do a full anisotropic analysis in Hyperworks and Solidworks. Wilburn's work did not consider Poisson's ratio and this analysis only estimated it for a single direction. Both programs require Young's Modulus and Poisson's ratio in all directions for anisotropic analysis. It was decided designing to a worst case scenario with a FoS would produce the most useful model. Further, anisotropic behavior is best modeled in the full version of Hyperworks using 3-D analysis. The version used here was the student version running a 2-D analysis.

The most useful part of this analysis will be in designing the eventual microgravity printer. This beam provides a way to estimate how much material the printer will need based on the maximum expected loading during operations. Additional benefits and shortcomings of this methodology and optimization will be found with further design of the orbital printer and missions it will support. Design of the printer should be done in tandem with this type of optimization, building off information from one another during the entire process.

V. Conclusions and Recommendations

5.1 Conclusions

5.1.1 Environmental Exposure and Testing

The main goal of this research and analysis was to see how ULTEM 9085's structural behavior changed with exposure to orbital conditions, specifically Ultraviolet (UV) radiation. The environmental exposure, while not an exact replica of Low Earth Orbit (LEO) conditions, did show that ULTEM 9085's structural characteristics changed with UV exposure. The only characteristic whose change was significant and directly attributable to UV exposure was the Fracture Strain. The Ultimate Tensile Strength (UTS) and Yield Tensile Strength (YTS) were influenced by the UV radiation but not as much as by the vacuum and elevated temperatures. Lastly, the change in Young's modulus' was mostly due to the vacuum and elevated temperatures, the UV potentially contributed but it is not possible to separate the UV and non-UV data.

Further, the UV likely hardened the outer few microns of the ULTEM 9085, reducing the variance in the collected values. This would have affected each characteristic regardless of whether they were changed by the UV radiation. Exposure to the orbital environment made the ULTEM 9085 stiffer and stronger, with the UV and vacuum both increasing overall strength and the UV specifically making the ULTEM 9085 more brittle.

However, aspects of the samples, the test setup, and the post-processing methodology prevented the gathering of as detailed information about Poisson's ratio and limited the usability of data. The high Coefficient of Variance (CoV) values across all properties is endemic of these issues, highlighting the inconsistency that is a common issue with Fused Deposition Modeling (FDM) parts and the methodology of this

study.

5.1.2 Optimization

A cylindrical beam's internal topology was successfully optimized for the given parameters. The topology was based on the aggregate of 9 possible load configurations to provide a general shape. Using a Factor of Safety (FoS) of 2 and volume reduction of 35%, the resulting maximum Von Mises stress and allowable end moment was calculated. It was assumed that the shear forces and the moment did not interact, leaving the shear stress and axial stress to be related only by the Von Mises criteria.

The optimization was designed to be as conservative as possible due to not having complete structural characteristics of ULTEM 9085 and a limited design basis. Specifically, the anisotropy of the ULTEM was not modeled in the software, so the the worst case structural strength was used when necessary. This optimization will assist in developing the autonomous 3-D printer and the structures it will be expected to print.

5.2 Future Recommendations

5.2.1 Environmental Exposure and Testing

Larger dogbones would be the best improvement for the environmental testing. FDM parts are typically larger than the dogbones used here and the effects of printing errors would be reduced. The surface hardening effects would also be more realistic, as a lower percentage of the material would be affected if the dogbones were larger. Along with the larger dogbones, changes in the test setup allowing for finer control over the UV exposure would improve consistency in exposure amounts. This could be either less samples under a single bulb or closer monitoring of the bulbs to reduce drift. Lastly, it is not necessary to expose the dogbones to multiple Sols of UV radiation for

several months. These same results could be found with a 1 Sol bulb and reducing the exposure time by 75%.

For testing, more types of testing would improve the accuracy of the structural characteristics, especially Poisson's ratio. The anisotropic nature of FDM makes this essential for complete understanding of UTLEM 9085. Testing dogbones printed in different directions like in Wiburn's research is the most essential next step to see if the orbital conditions affect all directions of ULTEM 9085 the same. Lastly, exactly how the UV radiation and the vacuum change the ULTEM 9085 should be characterized, such as seeing how deep the surface hardening is and if any ULTEM 9085 is diffused due to the vacuum.

5.2.2 Optimization

There is no standard structural model for printed anisotropic ULTEM 9085. The best way to improve the accuracy of the optimization would be to have a Young's Modulus and Poisson's ratio for each direction based on how the ULTEM 9085 is printed. This requires much more experimentation in line with what was outlined in the previous section. Using a single software package could improve accuracy by ensuring all calculations are done with the same underlying computational assumptions. More types of elements and meshes should be used in optimizing the beam. A full 3-D model of the entire beam with all loading applied simultaneously would be the best optimization setup but would depend on having all of ULTEM 9085's entire structural characteristics. Looking at the algorithm, the design variable vector should be changed to mass. Mass is the main limiting factor for space operations and a lower mass design is preferable for most missions. The penalization power could also be adjusted to remove more or less material. Finally, having a more specific design for the printer and mission would help in selecting an accurate loading pattern.

Appendix A. Dogbone Fracturing and Cross Sections

Table A.1. The fracture location for each sample.

Sample #	1	2	3	4	5	6	7	8
Set 1	Neck	Root	Root	Root	Neck	Neck	Neck	Root
UV Sets								
Set 2	Neck	Neck	Neck	Neck	Neck	Neck	Neck	Neck
Set 6	Neck	Neck	Neck	Neck	Neck	Neck	Neck	Neck
Set 4	Neck	Neck	Neck	Neck	Neck	Neck	Neck	Neck
Set 8	Neck	Neck	Neck	Neck	Neck	Neck	Neck	Neck
non-UV Sets								
Set 3	Neck	Root	Neck	Neck	Root	Root	Neck	Root
Set 5	Neck	Root	Root	Root	Root	Root	Neck	Root
Set 7	Neck	Neck	Root	Root	Root	Neck	Root	Neck
Set 9	Neck	Root	Root	Root	Root	Root	Neck	Neck

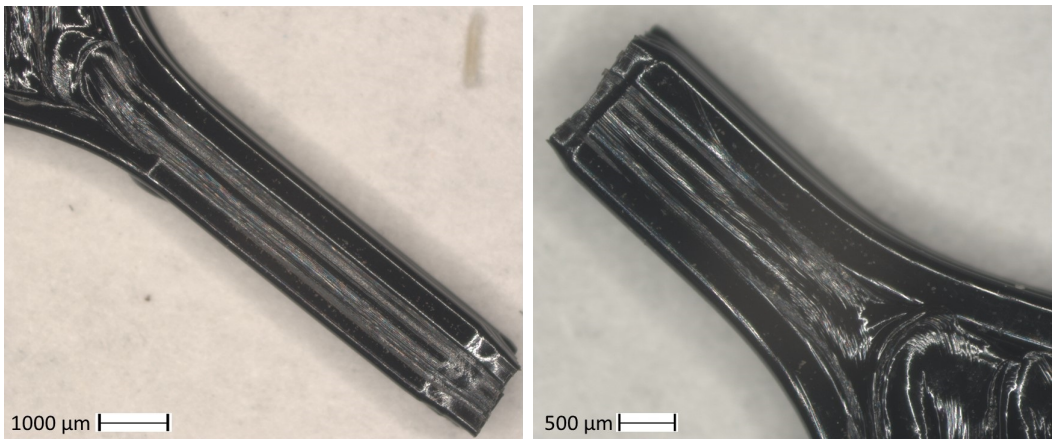

Figure A.1. The two halves of a neck fracture.

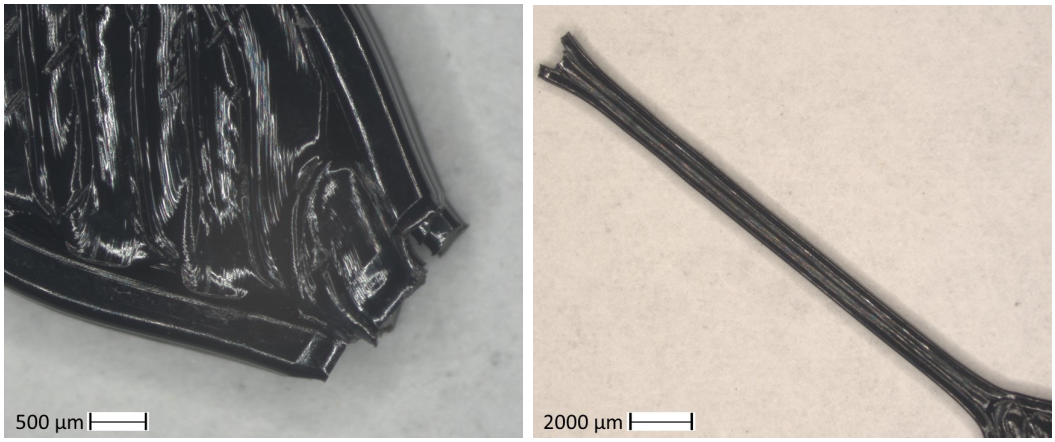

Figure A.2. The two halves of a root fracture.

The following cross-sections best highlight the surface hardening 'scratches,' visible on the center of the lower edge.

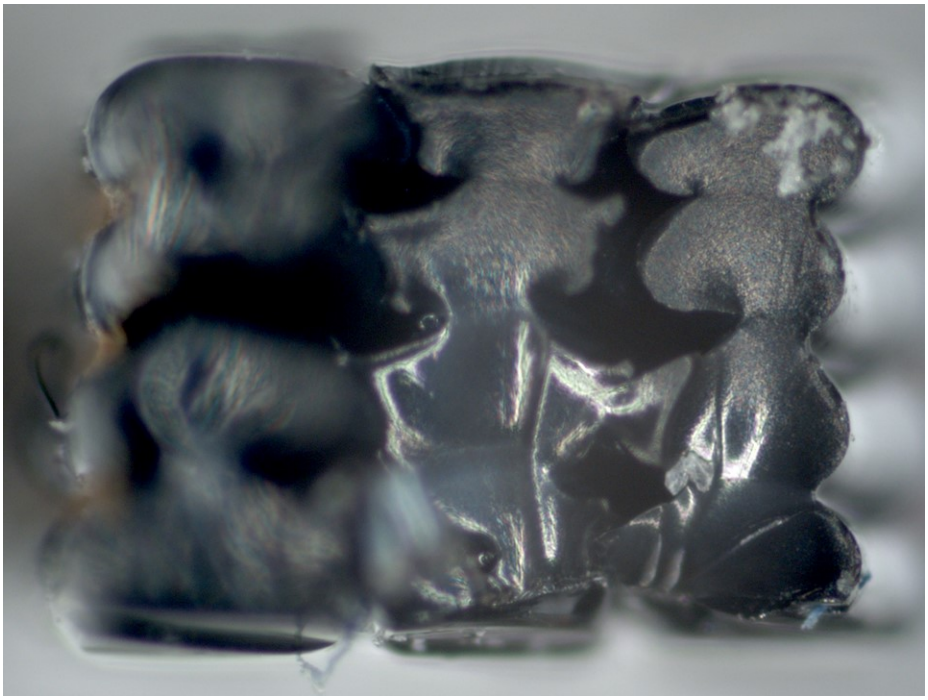

Figure A.3. The cross-section area of Dogbone 1 from Set 6

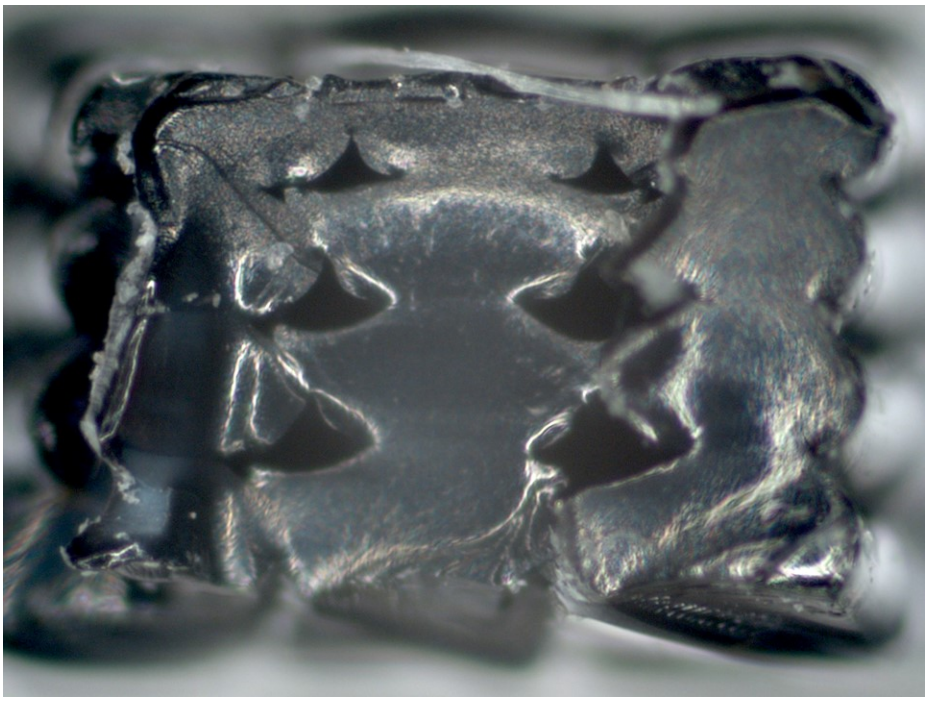

Figure A.4. The cross-section area of Dogbone 3 from Set 6

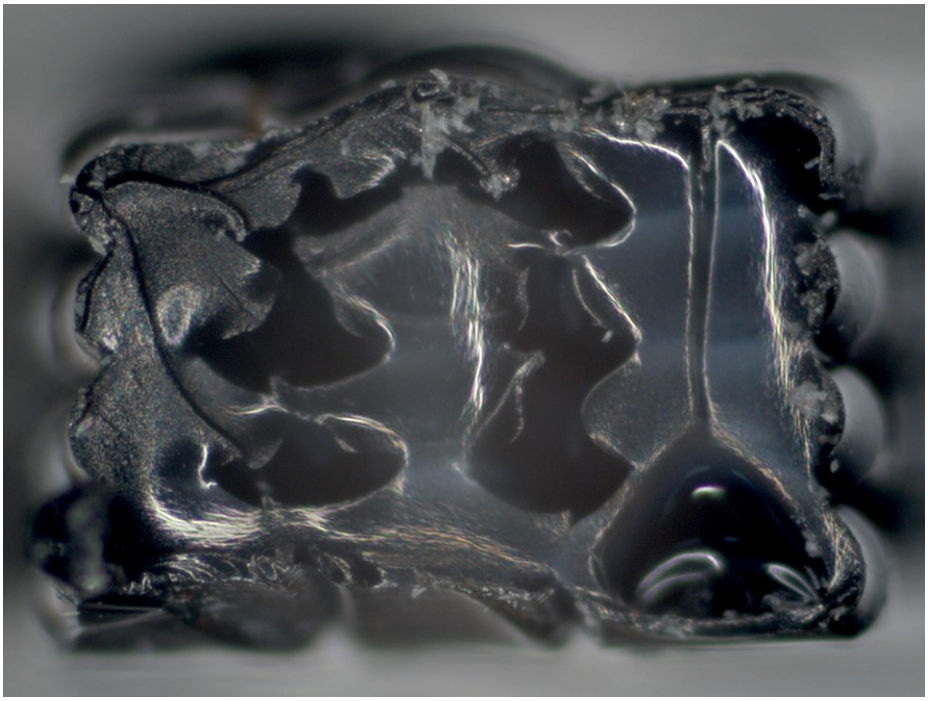

Figure A.5. The cross-section area of Dogbone 6 from Set 6

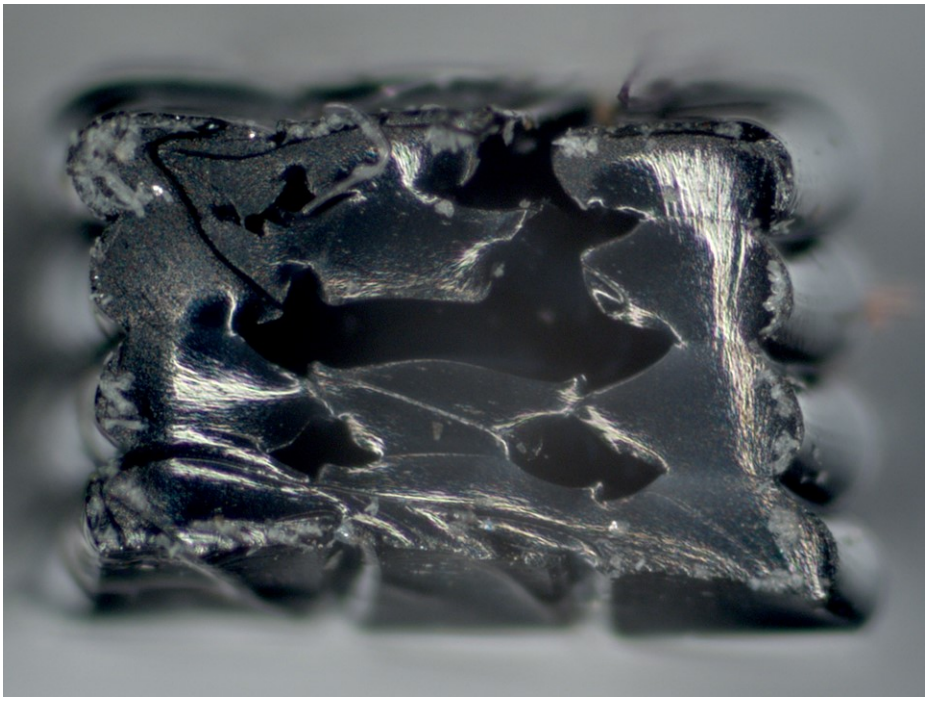

Figure A.6. The cross-section area of Dogbone 7 from Set 6

Appendix B. Topology Results

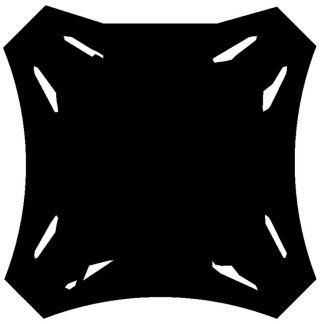

Figure B.1. STL result for Load Configuration 1

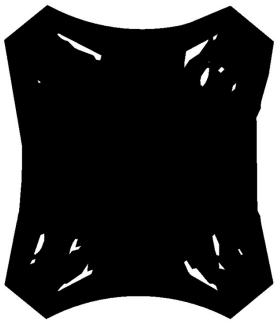

Figure B.2. STL result for Load Configuration 2

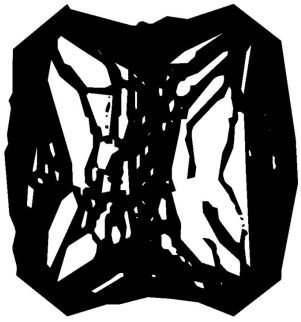

Figure B.3. STL result for Load Configuration 3

Figure B.4. STL result for Load Configuration 4

Figure B.5. STL result for Load Configuration 5

Figure B.6. STL result for Load Configuration 6

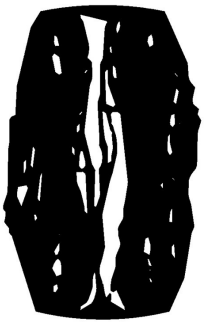

Figure B.7. STL result for Load Configuration 7

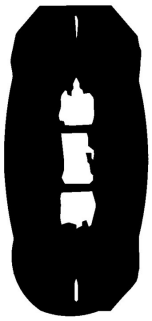

Figure B.8. STL result for Load Configuration 8

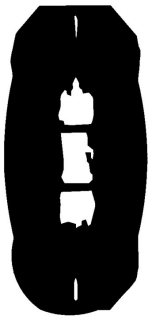

Figure B.9. STL result for Load Configuration 9

Bibliography

[1] W. E. Masters, "Computer automated manufacturing process and system," Patent US4 665 492A, 5 12, 1984.

[2] S. S. Shipp *et al.*, "Emerging global trends in advanced manufacturing," Institute for Defense Analysis, Tech. Rep., March 2012.

[3] Z. A. Wilburn, "Manufacture of fused deposition modeling joints using ultem 9085," Master's Thesis, Air Force Institute of Technology, March 2019.

[4] S. Loff, "International space station's 3-d printer," August 2017. [Online]. Available: https://www.nasa.gov/content/international-space-station-s-3-d-printer

[5] D. Adams, "Cosmonauts launch 3d-printed satellite from the international space station," August 2017. [Online]. Available: https://www.digitaltrends.com/cool-tech/3d-printed-satellite-iss/

[6] *ULTEM 9085 PRODUCTION - GRADE THERMOPLASTIC FOR FORTUS 3D PRODUCTION SYSTEMS*, Stratasys, 7665 Commerce Way, Eden Prairie, MN, 55344, 2016.

[7] J. P. McCrea, "Design of a zero-gravity, vacuum-based 3d printer robot for in-space satellite assembly," Master's Thesis, Air Force Institute of Technology, March 2018.

[8] X. Yan and P. Gu, "A review of rapid prototyping technologies and systems," *Computer-Aided Design*, vol. 28, no. 4, pp. 310–311, 1996.

[9] *Fortus 380mc and 450mc*, 7665 Commerce Way, Eden Prairie, MN 55344, 2018. [Online]. Available: www.stratasys.com

[10] A. Bagsik and V. Schöppner, "Mechanical properties of fused deposition modeling parts manufactured with ultem*9085," *ANTEC*, 2011.

[11] J. T. Cerri, "Thermal testing of fused deposition modeling extended to an orbital environment," Master's Thesis, Air Force Institute of Technology, August 2018.

[12] E. M. Silverman, "Space enviromental effects on spacecraft: Leo materials selection guide," NASA, Tech. Rep., August 1995.

[13] H. R. Gloria *et al.*, "Initial weight loss of plastics in a vacuum at temperatures from 80° to 500° f," Nation Aeronautics and Space Administration, Tech. Rep., December 1962.

[14] Y. C. Ching *et al.*, *Durability and Life Prediction in Biocomposites, Fibre-Reinforced Composites and Hybrid Composites*. Woodhead Publishing, 2019, ch. 18: Effects of high temperature and ultraviolet radiation on polymer composites, pp. 412–414, 418–422.

[15] H. Evans *et al.*, *The Phenomenology of Intelligence-focused Remote Sensing Volume 1: Electro-optical Remote Sensing*, 1st ed., T. Renner, Ed. 156 William Street, 9th Floor, New York, NY 10038: Riverside Research, 2014.

[16] A. Boubakri *et al.*, "Study of uv-aging of thermoplastic polyurethane material," *Materials Science and Engineering*, vol. 527, pp. 1649–1654, 2010.

[17] J. Lohr and J. Parker, "An analytical method for evaluating the effects of radiation in vacuum on the mechanical properties of rigid plastics," Nation Aeronautics and Space Administration, Tech. Rep., 1963.

[18] J. H. Chaudet *et al.*, "Mechanisms of ultraviolet stabilization of plastics," *SPE TRANSACTIONS*, pp. 27–28, 1961.

[19] T. L. Bergman *et al.*, *Fundamentals of Heat and Mass Transfer*, 7th ed., L. Ratts, Ed. John Wiley and Sons, Inc, 2011.

[20] *ORIEL PRODUCT TRAINING Spectral Irradiance*, Newport, 1791 Deere Avenue, Irvine, California 92606.

[21] O. Sigmund, "Topology optimization: a tool for the tailoring of structures and materials," *Philosophical Transactions of The Royal Society A*, 2000.

[22] W. T. Graves, "Topology optimization of a penetrating warhead," Master's Thesis, Air Force Institute of Technology, March 2016.

[23] O. Sigmund, "A 99 line topology optimization code written in matlab," *Struct. Multidisc. Optim.*, no. 21, pp. 120–127, 2001.

[24] L. Dede and T. J. H. Michael J. Borden, "Emerging global trends in advanced manufacturing," Institute for Computational Engineering and Sciences, Tech. Rep., September 2011.

[25] *ASTM D638-14, Standard Test Method for Tensile Properties of Plastics*, West Conshohocken, PA, 2014. [Online]. Available: www.astm.org

[26] J. R. Wertz *et al.*, Eds., *Space Mission Engineering: The New SMAD*, 1st ed. 490 W. 147th Street, Hawthorne, CA 90250: Microcosm Inc., 2011.

[27] "Dobot cr5," 2020. [Online]. Available: https://www.dobot.cc/industrial-robotics/dobot-cr5-overview.html

[28] *Lulzbot TAZ 6 Specifications*, Aleph Objects, Inc., USA.

REPORT DOCUMENTATION PAGE

Form Approved
OMB No. 0704-0188

1. REPORT DATE *(DD-MM-YYYY)*	**2. REPORT TYPE**	**3. DATES COVERED** *(From - To)*
26-03-2020	Master's Thesis	April 2019 to Feb 2020

4. TITLE AND SUBTITLE
Investigation Of ULTEM 9085 For Use In 3-D Printed Orbital Structures

5a. CONTRACT NUMBER

5b. GRANT NUMBER

5c. PROGRAM ELEMENT NUMBER

6. AUTHOR(S)
Gallagher, William R, Mr, GS-11

5d. PROJECT NUMBER

5e. TASK NUMBER

5f. WORK UNIT NUMBER

7. PERFORMING ORGANIZATION NAME(S) AND ADDRESS(ES)
Air Force Institute of Technology
Graduate School of Engineering and Management (AFIT/EN)
2950 Hobson Way
Wright-Patterson AFB OH 45433-7765

8. PERFORMING ORGANIZATION REPORT NUMBER
AFIT-ENY-MS-20-M-262

9. SPONSORING/MONITORING AGENCY NAME(S) AND ADDRESS(ES)
Intentionally Left Blank

10. SPONSOR/MONITOR'S ACRONYM(S)

11. SPONSOR/MONITOR'S REPORT NUMBER(S)

12. DISTRIBUTION/AVAILABILITY STATEMENT
DISTRIBUTION STATEMENT A.
APPROVED FOR PUBLIC RELEASE; DISTRIBUTION IS UNLIMITED.

13. SUPPLEMENTARY NOTES
This work is declared a work of the U.S. Government and is not subject to copyright protection in the United States.

14. ABSTRACT
This thesis explored two areas: how the structural characteristics of ULTEM 9085 changed after exposure UV radiation and the required design of an ULTEM 9085 beam to be 3-D printed in microgravity. ULTEM 9085 dogbones were printed and exposed to several Sol's worth of UV radiation in a vacuum chamber. Axial testing showed the ULTEM 9085 became stronger as a result of the vacuum and more brittle as a result of the UV radiation. Simultaneously, a cylindrical beam's internal structure was optimized based on several possible loading configurations expected during printing on orbit.

15. SUBJECT TERMS
Additive Manufacturing, UTLEM 9085, Space, Ultraviolet, Structural Testing

16. SECURITY CLASSIFICATION OF:			**17. LIMITATION OF ABSTRACT**	**18. NUMBER OF PAGES**	**19a. NAME OF RESPONSIBLE PERSON**
a. REPORT	**b. ABSTRACT**	**c. THIS PAGE**			Dr. Carl Hartsfield, AFIT/ENY
U	U	U	UU	75	**19b. TELEPHONE NUMBER** *(Include area code)* (937) 255-3636 x 4667 Carl.Hartsfield@afit.edu